Middle to late Eocene exhumation of the Greater Himalayan Sequence in the Central Himalayas: Progressive accretion from the Indian plate

Published version:

DOI:10.1130/B31471.1

(Article begins on next page)

The Geological Society of America Bulletin

Middle to late Eocene exhumation of the Greater Himalayan Sequence in the Central Himalayas: progressive accretion from the Indian plate

--Manuscript Draft--

Manuscript Number:	B31471
Full Title:	Middle to late Eocene exhumation of the Greater Himalayan Sequence in the Central Himalayas: progressive accretion from the Indian plate
Short Title:	Eocene exhumation of the Greater Himalayan Sequence, Nepal Himalaya
Article Type:	Article
Keywords:	Himalaya, Exhumation, Greater Himalayan Sequence, monazite geochronology, pseudosections, P-T-t-D paths, Kalopani shear zone, in-sequence shearing, Kali Gandaki valley
Corresponding Author:	Chiara Montomoli, Ph.D. Università di Pisa Pisa, Pisa ITALY
Corresponding Author's Institution:	Università di Pisa
First Author:	Rodolfo Carosi, Professor
Order of Authors:	Rodolfo Carosi, Professor
	Chiara Montomoli, Professor
	Salvatore Iaccarino, PhD
	Hans-Joachim Hans-Joachim, Professor
	Daniela Rubatto, Professor
	Antonio Langone, PhD
	Lorenzo Gemignani, Dr
	Dario Visonà, Professor
Abstract:	In the Kali Gandaki valley (central Nepal), a ductile, high-temperature, contractional shear zone with a top-to-the-SW sense of shear, known as Kalopani Shear zone (KSZ), is located within the uppermost part of the Greater Himalayan Sequence (GHS). We mapped and investigated this shear zone in in detail, in order to unravel its age and role in the evolution of the GHS. Pseudosection modeling and inverse geothermobarometry reveal that rocks involved in the KSZ experienced pressure-temperature conditions between 0.6-0.85 GPa and 600-660°C. U-Th-Pb in-situ LA-ICP-MS and SHRIMP dating on monazite point to retrograde metamorphism related to the KSZ starting from ~ 41-30 Ma. The kinematics of the KSZ and associated erosion and/or tectonics, caused the Middle-Late Eocene exhumation of the GHS in the hanging wall of the KSZ zone at least nine million years before the activities of the High Himalayan Discontinuity, the Main Central Thrust, and the South Tibetan Detachment. Structural data, metamorphic conditions and geochronology from the KSZ, compared to those of other major tectonic discontinuities active within the GHS in the Kali Gandaki valley, indicate that shear deformation and exhumation were not synchronous but migrated downward and southward at different lower levels within the GHS. These processes caused the exhumation of the hanging-wall rocks of the activated shear zones. The main consequence of this tectonic is that exhumation was driven by an in-sequence shearing mechanism progressively involving new slices of the Indian crust and not solely by the coupled activity of Main Central Thrust and South Tibetan Detachment.
Suggested Reviewers:	Delores M. Robinson, Professor Associate professor, University of Alabama dmr@ua.edu Expert of tectonics of the Himalaya and Tibet since at least 20 years

	Matthew J. Kohn, Professor Professor, Boise State University, USA mattkohn@boisestate.edu Expert in monazite geochronology, petrology, Himalayan geology and exhumation of the crystalline core of the belt.
	Igor M. Villa, Professor Professor, Universitat Bern igor.villa@geo.unibe.ch High-level expertise in geochronology and wide knowledge of Himalayan geology
	Jean Luc Epard, PhD Associate professor, University of Lausanne Jean-Luc.Epard@unil.ch Expertise in structural geology and tectonics of the Alps and Himalayas
	Enrico Tavarnelli, Professor Professor, Universita degli Studi di Siena enrico.tavarnelli@unisi.it Expertise of structural geology and tectonics of collisional belts
Opposed Reviewers:	Mike P. Searle, Professor Professor, University of Oxford mikes@earth.ox.ac.uk Opposite view of the exhumation mechanisms of the crystalline core of the Himalaya leading sometimes to refuse a manuscript without reviewing it.

Middle to late Eocene exhumation of the Greater Himalayan Sequence in the Central Himalayas: progressive accretion from the Indian plate

Rodolfo Carosi[1], Chiara Montomoli[2], Salvatore Iaccarino[2], Hans-Joachim Massonne[3], Daniela Rubatto[4,5], Antonio Langone[6], Lorenzo Gemignani[7] and Dario Visonà[8]

[1] *Dipartimento di Scienze della Terra, Università di Torino, Italy, rodolfo.carosi@unito.it*
[2] *Dipartimento di Scienze della Terra, Università di Pisa, Italy, chiara.montomoli@unipi.it, iaccarino@dst.unipi.it*
[3] *Institut für Mineralogie und Kristallchemie, Universität Stuttgart, Germany, h-j.massonne@imi.uni-stuttgart.de.*
[4] *Research School of Earth Sciences, Australian National University, Canberra, Australia,*
[5] *Institute of Geological Sciences, University of Bern, Balzerstrasse 1-3, 3012 Bern, Switzerland daniela.rubatto@geo.unibe.ch*
[6] *Istituto di Geoscienze e Georisorse, C.N.R., Pavia, Italy, langone@crystal.unipv.it*
[7] *Department of Earth Science, Faculty of Earth and Life Sciences Vu University, The Netherlands, l.gemignani@vu.nl*
[8] *Dipartimento di Geoscienze, Università di Padova, Italy, dario.visona@unipd.it*

ABSTRACT

In the Kali Gandaki valley (central Nepal), a ductile, high-temperature, contractional shear zone with a top-to-the-SW sense of shear, known as Kalopani Shear zone (KSZ), is located within the uppermost part of the Greater Himalayan Sequence (GHS). We mapped and investigated this shear zone in in detail, in order to unravel its age and role in the evolution of the GHS.

Pseudosection modeling and inverse geothermobarometry reveal that rocks involved in the KSZ experienced pressure-temperature conditions between 0.6-0.85 GPa and 600-660°C. U-Th-Pb in-situ LA-ICP-MS and SHRIMP dating on monazite point to retrograde metamorphism related to the KSZ starting from ~ 41-30 Ma. The kinematics of the KSZ and associated erosion and/or tectonics, caused the Middle-Late Eocene exhumation of the GHS in the hanging wall of the KSZ zone at least nine million years before the activities of the High Himalayan Discontinuity, the Main Central Thrust, and the South Tibetan Detachment.

Structural data, metamorphic conditions and geochronology from the KSZ, compared to those of other major tectonic discontinuities active within the GHS in the Kali Gandaki valley, indicate that shear deformation and exhumation were not synchronous but migrated downward and southward at different lower levels within the GHS. These processes caused the exhumation of the hanging-wall rocks of the activated shear zones. The main consequence of this tectonic is that exhumation was driven by an in-sequence shearing mechanism progressively involving new slices of the Indian crust and not solely by the coupled activity of Main Central Thrust and South Tibetan Detachment.

Key words: Himalaya, Exhumation, Greater Himalayan Sequence**,** monazite geochronology, pseudosections, P-T-t-D paths, Kalopani shear zone, in-sequence shearing, Kali Gandaki valley.

1. INTRODUCTION

The understanding of exhumation mechanisms of deep-seated metamorphic rocks in collisional orogens has been greatly improved by the discovery of contemporaneous contractional and normal-sense shear zones in the same vertical section in orogenic belts. The normal sense top-to-the-NE South Tibetan Detachment (STD) and the contractional top-to-the-SW Main Central Thrust (MCT), bounding the crystalline core of the belt, the Greater Himalayan Sequence (GHS), in the Himalayas, to the top and to the bottom respectively, are regarded as the most classic example of a coupled tectonic system of faults/shear zones acting contemporaneously with opposite kinematics (Burchfiel et al., 1992; Hodges et al., 1992) in the time span between ~23 and 17 Ma (Godin et al., 2006). The GHS, one of the major tectonic units in the Himalayan belt, is composed of medium- to high-grade metamorphic rocks and exposed for nearly 2400 km along the orogen (Hodges, 2000; Yin 2006 with references). This unit has been regarded as a continuous and coherent slice and attention has been paid almost exclusively on the boundary shear zones/faults, especially when formulating tectonic and exhumation models related to: i) channel flow (Beaumont et al., 2001; Grujic, 2006), ii) wedge extrusion (Hodges et al., 1996; Grujic et al., 1996), iii) channel flow followed by extrusion (Godin et al., 2006; Cottle et al. 2015 with references), iv) wedge insertion (Webb et al., 2007), and v) critical taper wedge (Kohn, 2008). Only in the critical taper wedge model the contemporaneous activity of the MCT and STD is not required.

Faults or shear zones inside the GHS, such as the Kakthang thrust in Bhutan (Daniel et al., 2003), the Kalopani shear zone (Nepal, Vannay and Hodges, 1996; Godin, 2003; Searle, 2010), the Modi Khola shear zone (Nepal, Hodges et al., 1996), and the Nyalam thrust (Nepal, Wang et al., 2013), have been interpreted as out-of-sequence thrusts (Mukherjiee et al., 2012 with references). In the last few years, growing evidence of the occurrence of shear zones and metamorphic discontinuities has been reported from several places within the GHS along the belt from western Nepal to Sikkim. A jump in the metamorphic conditions, between the upper portion of the GHS and the lower GHS, has been reported by several authors (Carosi et al., 2007, 2010; Groppo et al., 2009; Corrie and Kohn, 2011; Yakymchuck and Godin, 2012; Imayama et al., 2012; Rubatto et al., 2013; Kohn et al., 2004; Kohn 2008; Larson et al., 2010, 2013, 2015; He et al., 2015; Montomoli et al., 2013, 2015 for a review; Cottle et al., 2015; Khanal et al., 2015; Iaccarino et al., 2015; Wang et al., 2015). Moreover, a regional-scale tectonic and metamorphic discontinuity, separating the upper GHS from the lower GHS – called the High Himalayan Discontinuity (HHD: Montomoli et al., 2013; 2015) – has been recognized in the Central Himalayas (Fig. 1a). The HHD was active before the activation of the MCT, since ~ 28-25 Ma, with a top-to-the-SW sense of shear. Here, we strictly follow the definition of the HHD proposed by Montomoli et al. (2013) avoiding referring to it as a "thrust" because it is a ductile shear zone.

The activation of the HHD triggered the early exhumation of the upper GHS in the Central Himalayas before the classical 23-17 Ma time span for the MCT-STD coupled activity (Montomoli et al., 2013; 2015). Despite an apparent partial overlap in the activity of the HHD and MCT, the HHD is always older and located in a higher structural position with respect to the MCT along the same section of the belt (Montomoli et al., 2015, Table 1). Iaccarino et al. (2015) reported the occurrence of a tectono-metamorphic discontinuity in the Kali Gandaki section, > 1 km north of the MCT at Dana village (Fig. 1) (Le Fort, 1975; Colchen et al., 1986; Vannay and Hodges, 1996). This discontinuity in the Kali Gandaki section correlates with the HHD in western Nepal and was active between 25 and 18 Ma (Iaccarino et al., 2015).

In order to unravel the tectonic and metamorphic history of the GHS we investigate a further ductile shear zone in the Kali Gandaki valley (Central Nepal): the Kalopani shear zone (KSZ; Vannay and Hodges, 1996) (Fig. 1b, 2), by detailed mapping, meso- and microstructural analyses, U-Th-Pb monazite dating, and pressure-temperature (P-T) pseudosection modelling. The KSZ is the structurally highest contractional top-to-the-SW shear zone up to now recognized in the GHS. According to $^{40}Ar/^{39}Ar$ cooling ages on white mica it was active before 15-13 Ma (Vannay and Hodges, 1996) and possibly also between 22.5 and 15 Ma (Godin et al., 2001).

Monazite radiometric dating in structural and metamorphic context resulted in older ages for the activity of the KSZ and for the exhumation of the uppermost part of the GHS, which cannot be explained by the most popular tectonic models proposed for the Himalaya. Therefore, we propose a different model of exhumation of the GHS that takes into account the older ages and the occurrence of three different shear zones within the GHS along the same transect.

2. GEOLOGICAL SETTING

2.1 Himalayan Units

The Himalayan mountain belt (Fig. 1a) evolved after the collision between the Asian and Indian continental plates at ~ 55-50 Ma (Hodges, 2000; Najman et al., 2010). This collision occurred after the break-up of Gondwana and the evolution of a long last-standing Andean-type active margin, caused by the subduction of Neo-Tethys oceanic crust below the Lhasa Block, accompanied by the intrusion of large granitoid bodies and accretion of arc terranes. The Himalayan belt is subdivided into four main tectonic zones, separated by regional-scale tectonic discontinuities that can be followed along the entire length of the belt (Gansser, 1964; Le Fort, 1975; Upreti, 1999; Hodges, 2000; Yin, 2006). In a north–south transect perpendicular to the belt in Nepal, these principal tectonic zones are from south to north, the Terai, the Siwalik (Sub-Himalayan), the Lesser Himalayan Sequence (LHS), the GHS and the Tethyan Sedimentary Sequence (TSS). The Terai unit is the northern edge of the alluvial plain of the Ganges and Indus rivers (Indo-Gangetic Plain), the foreland basin of the Himalaya with the most recent alluvial sediments (Upreti, 1999). The Sub-Himalayan unit (Siwalik Group) represents the foreland basin, made up by a Tertiary molasse in a sedimentary sequence that varies from 2 to 10 km in thickness (DeCelles et al., 1998; Upreti, 1999; White et al., 2002; Szulc et al., 2006).

The LHS is bound at the base by the Main Boundary Thrust and at the top by the MCT, a regional thrust sense shear zone (Fig. 1a) which separates it from the overlying GHS. Both thrusts show a top-to-the-S sense of movement. Since the MCT is not a single thrust, but a thick ductile to brittle shear zone, with a variable thickness (100 m up to several km: Searle et al., 2008), it is often referred as the Main Central Thrust Zone (MCTZ) to identify the package of sheared rocks.

According to Stephenson et al. (2001) both GHS and LHS rocks are ductilely sheared by the MCT activity, with the latter ductilely incorporated in the MCTZ during the shear zone activity.

The LHS mainly consists of lower greenschist- to lower amphibolite-facies clastic metasedimentary rocks, organized according to a structurally complex system of fold-and-thrust nappes (De-Celles et al., 1998; Robinson & Martin, 2014). The original sedimentary pile was 8–10 km thick, as suggested by Schelling (1992) using palinspastic reconstructions. The predominant rock types are impure quartzite and psammitic slate, phyllite and schist, with subordinate impure marble, metamorphosed mafic rock and augen gneiss (Upreti, 1999; Hodges, 2000; Yin, 2006).

The GHS, a continuous belt of Late Proterozoic to Cambro-Ordovician medium- to high-grade metasedimentary and metaigneous rocks with associated Miocene leucogranites (Le Fort, 1975; Carosi et al., 1999; Upreti, 1999; Hodges, 2000; Visonà and Lombardo, 2002; Yin, 2006; Visonà et al., 2012), represents the metamorphic core of the Himalaya, forming the central part of the belt, and is often associated with the highest topographic relief.

The uppermost tectonic domain to the north is the TSS, which is tectonically separated from the lower GHS by a system of normal faults and ductile shear zones (STDS) (Caby et al., 1983; Burg et al., 1984; Burchfiel et al., 1992; Carosi et al., 1998, 2002; Law et al., 2004; Searle, 1999; 2010) active up to 13-11 Ma in the eastern Himalaya (Kellett et al., 2009; Montomoli et al., 2015). The TSS comprises a nearly continuous sequence of Palaeozoic to Eocene sediments, which were deposited on the northern passive margin of the Indian plate (Gaetani and Garzanti, 1991). The rocks of the TSS experienced mostly very low-grade metamorphic conditions. A higher metamorphic grade corresponding to the greenschist facies up to the lower amphibolite facies occurs only at the base of the sequence in the Cambro-Ordovician rocks affected by the activity of STDS (Godin et al., 1999; Crouzet et al., 2007; Antolìn et al., 2011; Dunkl et al., 2011) and in other sporadic localities (Montomoli et al., in press). To the north, the TSS is bounded by flysches and ophiolites (often with a blueschist metamorphic imprint) of the Indus-Tsangpo suture zone.

2.2 The Greater Himalayan Sequence

The GHS has been classically subdivided into three litho-tectonic units (Le Fort, 1975; Colchen et al., 1986; Vannay and Hodges, 1996; Searle and Godin, 2003; Carosi et al., 2014):

- Unit 1 is the base of the GHS consisting predominantly of clastic metasedimentary rock, such as biotite-muscovite-garnet-kyanite gneiss, and subordinate micaschist and phyllite, calc-schist, quartzite, and migmatitic gneiss (Hodges, 2000; Carosi et al., 2014, 2015; Iaccarino et al., 2015). Unit 1 has been traditionally considered as a uniform crustal section with a variable thickness from 1 km to more than 20 km along strike (Le Fort, 1975). Iaccarino et al. (2015) describe the presence of a tectono-metamorphic discontinuity active at 25-18 Ma and correlated it with the HHD of Montomoli et al. (2015) dividing unit 1 in two sub-units.
- Unit 2. A 2-4 km thick sequence of amphibolite-facies, banded calc-silicate gneiss, paragneiss, marble and amphibolite represents unit 2. The boundary between units 1 and 2 is parallel to the compositional layers in both units. Its transition is gradual and highlighted by changes in mineral composition.
- Unit 3. Orthogneiss, migmatite and minor marble, metapelite and calc-silicate make up unit 3 (Vannay and Hodges, 1996; Godin et al., 2001; Searle, 2010). The orthogneiss is Cambrian-Ordovician in age (Godin et al., 2001) and was intruded by a network of Miocene sills and leucogranitic dykes. Isotopic Rb-Sr data indicate that the protoliths of unit 3 are entirely Cambrian-Ordovician in age (Pognante et al., 1990) in agreement with U-Pb zircon and monazite ages (Godin et al., 2001). The uppermost part of unit 3 was affected by the Annapurna Detachment (Fig. 1b), a strand of the STDS. Unit 3 includes the Largjung Formation (Colchen et al., 1986), characterized by poly-deformed metapelites and marbles (Colchen et al., 1986; Vannay and Hodges, 1996). The orthogneiss was affected by the ductile KSZ (Vannay and Hodges, 1996; Godin et al., 2001; Godin et al., 2003; Searle, 2010; Carosi et al., 2014) (Fig. 1b). This zone is mainly characterized by highly strained orthogneiss and migmatitic gneiss, with a top-to-the-S sense of shear.

The main fabric in the GHS is a pervasive transposition foliation formed during a second deformation phase (S_2; Vannay and Hodges, 1996; Carosi et al., 2010, 2014, 2015; Iaccarino et al., 2015). This fabric is often recognizable as a shear band cleavage as defined by Passchier and Trouw (2005). The GHS in the Kali Gandaki valley (Fig. 1b) shows a homoclinal attitude (Brown and

Nazarchuk, 1993; Vannay and Hodges, 1996). The S_2 foliation typically strikes NW-SE and dips 30°–60° toward the NE. It is marked by the preferred orientation of metamorphic minerals and recrystallized quartz ribbons. Kyanite, staurolite, white mica, and biotite are occasionally bent or kinked along shear bands. Top-to-the-S/SW sense of shear is marked by C-S fabric, shear bands, asymmetric tails around porphyroclasts, and rotated garnets within the mylonites of the lower portion of the GHS affected by the deformation of the MCTZ. The elongation lineation (L_2) trends NE-SW and plunges NE (20°-60°). S_1, formed during D1 deformation, is sometimes preserved as a relict in D2 fold hinges (F_2) and S_2 microlithons and as internal foliation in porphyroblasts (Carosi et al., 2010; Vannay and Hodges, 1996).

The GHS at the regional scale underwent at least two later folding phases, characterized by nearly orthogonal NW - SE and NE - SW trending fold axes, resulting in kilometer-scale open folds with steeply dipping axial planes. These folds, well-exposed in western Nepal, affected the tectonic boundaries (Upreti, 1999; Carosi et al., 2002, 2007; Antolin et al., 2012) and have also been described eastward in the Mt. Everest-Mt. Makalu region, Sikkim and Bhutan (Lombardo et al., 1993; Carosi et al., 1999; Schelling, 1992).

3. THE KALOPANI SHEAR ZONE

The upper part of the GHS in the Kali Gandaki valley (Fig. 2) consists of orthogneisses (Fig. 3), paragneisses, micaschists, and calsilicates (Bordet et al., 1971; Colchen et al., 1980, 1986; Brown and Nazarchuk, 1993; Vannay and Hodges, 1996; Godin, 2003; Searle, 2010; Carosi et al., 2014). The sequence is affected by a 20-50 m thick ductile shear zone, the KSZ (Vannay and Hodges, 1996; Carosi et al., 2014) (Fig. 1b, 2), which crops out ~ 1 km north of Kalopani village and can be followed for at least 4-5 km to the SE, south of the village of Taglung (Figs.1b, 2). It is hosted in augen gneisses, paragneisses and micaschists and strikes NW-SE moderately dipping to the NE. The elongation lineation trends NE-SW and plunges 30°-40° to the NE (Fig. 2). Deflected foliation, S-C-C' fabric, mica-fish and sigma-type porphyroclasts (Fig. 3) confirm the top-to-the-SW sense of shear proposed by previous authors (Vannay and Hodges, 1996; Godin, 2003; Carosi et al., 2014).

Two samples from the shear zone (KL-21 and KL-19; Fig. 2) have been investigated for metamorphic evolution and geochronology of monazite. Sample KL-21 is a two mica-bearing orthogneiss (Fig. 3, 4) whereas sample KL-19 is a garnet-staurolite-bearing paragneiss (Fig. 4). Both samples show a coarse-grained spaced anastomozing foliation (S_2) outlined mainly by the dynamic recrystallization of biotite, muscovite, and quartz (Fig. 4). In both samples porphyroclasts, represented by feldspars in KL-21 and by garnet and staurolite in KL-19, are wrapped around by the

main foliation (Fig. 4). Garnet has pre-kinematic cores (Fig. 4a–b) that are enriched in inclusions of magnetite, ilmenite, quartz and chlorite, defining an internal foliation (S_i), which is discordant with the main external foliation (S_e). The garnet rims are inclusion-free. Staurolite porphyroclasts are boudinaged with recrystallization of biotite between boudin necks.
Microstructures in both samples point to a high-temperature deformation regime. Lobate grain boundaries between quartz and quartz/feldspar and pinning and window microstructures, which developed between quartz and biotite crystals (Fig. 4c–d), indicate a grain boundary migration mechanism for quartz recrystallization (Passchier and Trouw, 2005). Chessboard extinction in quartz (Carosi et al., 2014) due to simultaneous activity of basal and prismatic slip systems or α–β quartz transition indicates a T of deformation ≥ 630°C (Passchier and Trouw, 2005). Myrmekites abundant in feldspar porphyroclasts developed in sample KL-21 and confirm a high-temperature deformation regime (Carosi et al., 2014). Main kinematic indicators at the microscale are mica fish (type 1, 4 and 5 of Passchier and Trouw, 2005), C-S fabric (Fig. 4a) and rare asymmetric myrmekites in feldspar. All kinematic indicators support a top-to-the-S sense of shear.

4. METAMORPHIC EVOLUTION

4.1 Analytical Methods

Mineral chemical compositions (except for monazite see below) and X-ray maps were acquired using a CAMECA SX100 electron microprobe (EMP) at the Institut für Mineralogie und Kristallchemie (Universität Stuttgart) equipped with five wavelength-dispersive spectrometers. For chemical analyses an accelerating voltage of 15 kV and a beam current of 15 nA were used. The beam spot size was 5 µm. Synthetic and natural standards were used for EMP calibration. The analytical uncertainties in the method applied are reported in Massonne (2012). X-ray maps were acquired by stepwise movement under an electronic beam of 50 nA and subsequent computer aided evaluation. Representative garnet X-ray maps and profiles are presented in Fig. 5. Selected chemical compositions of the main phases are reported in Table 1. KL-19 bulk rock composition was obtained with XRF analyses of thin section chip at the Dipartimento di Scienze della Terra (Università di Pisa), following the analytical protocol of Tamponi et al. (2002).

4.2 Strategy to estimate P-T conditions

In order to constrain the metamorphic evolution of paragneiss KL-19, a P-T pseudosection has been constructed with the software PERPLE_X (Connolly, 2005) in the MnNCKFMASHTO system and

in the P-T range of 0.3-1.3 GPa and 400-800 °C, respectively (Fig. 6). The bulk rock composition used for the pseudosection is (in wt%) SiO_2 = 67.08, TiO_2 = 0.60, Al_2O_3 = 11.23, F_2O_{3tot} = 15.42, MgO = 1.76, MnO = 0.04, CaO = 0.55, Na_2O = 0.80, K_2O = 1.86, P_2O_5 = 0.09, LOI = 0.41. The rock composition is very high in iron and falls in the Fe-sand field of Herron (1988).
Since sample KL-19 contains magnetite and ilmenite as opaque minerals, the assumption of total iron as bivalent is not supported and some amount of trivalent iron must be considered. The observed modal amount of magnetite determined by point counting under reflected light yielded 5 % volume. Thus, at least ~35% of the total iron must be trivalent iron.
The calculations were performed with the internally consistent thermodynamic dataset of Holland and Powell (1998, and updates) and a CORK EoS for H_2O. The following solid-solution models were used: GlTrTsPg for amphibole, TiBio(HP) for biotite, Gt(HP) for garnet, Ctd(HP) for chloritoid, Pheng(HP) for K-white mica (with a maximum paragonite content of 50% mol), St(HP) for staurolite, hCrd for cordierite, Chl(HP) for chlorite, Ep(HP) for epidote, Omph(HP) for clinopyroxene, Mica(M) for Na-Ca rich white mica, IlGkPy for ilmenite, Opx(HP) for orthopyroxene, MtUl(A) for magnetite, melt(HP) for haplogranitic melt and feldspar models as described in Massonne (2012). H_2O was considered as a pure phase.

Finally, in order to check the consistency of the results obtained with the P-T pseudosection, the THERMOCALC average P-T (Powell and Holland, 1994) method was applied to equilibrated mineral rims (see also Vance and Mahar, 1998) and coupled with fluid-independent geothermometers such as the Ti-in biotite thermometry of Henry et al. (2005) for syn-S_2 biotite. Calculations with THERMOCALC were conducted using the 3.33 version and the internally consistent dataset of Holland and Powell (1998). The activities of the mineral end-members were calculated using the A-X software by Holland (http://www.esc.cam.ac.uk/research/research-groups/holland/ax). Since the THERMOCALC P–T estimates are dependent on the fluid composition (H_2O-CO_2), they can be used to obtain information on this parameter. For sample KL-19, a good overlap between estimates from the pseudosection, garnet-biotite thermometry, Ti-in-biotite thermometry with THERMOCALC average P-T was obtained for XH_2O = 1 (see below).

4.3 Mineral compositions and P-T results

X-ray maps (Fig. 5) of garnet grains from sample KL-19 show a decrease of Mn and Ca balanced by an increase of Mg from core to the inner rim. The outermost part of the rim shows lower Mg and somewhat higher Ca contents. This garnet domain was corroded suggesting garnet resorption. This is confirmed by a slight increase in Mn and Fe/(Fe+Mg) (i.e. Fe#, e.g. Spear, 1993; Fig. 5b). Chlorite enclosed in garnet is characterized by Mg/(Mg+Fe) = XMg of 0.42 (Table 1). The compositions of other phases in the matrix are relatively homogeneous. Si contents in white mica vary between 3.13 to 3.08 per formula unit (p.f.u.) whereas XMg in staurolite systematically decreases from core (0.15) to rim (0.12) (Table 1). Matrix biotite shows XMg and Ti (p.f.u.) of 0.39–0.43 and 0.12–0.14 p.f.u, respectively, which are systematically different from values of biotite included in garnet (XMg = 0.50–0.56 and Ti = 0.7–0.11 p.f.u.). Plagioclase is rich in the albite component with XAb (i.e. Na/(Na+Ca)) of 0.82–0.84.

According to the calculated pseudosection the observed paragenesis garnet-staurolite-biotite-white mica-plagioclase-quartz-magnetite-ilmenite in sample KL-19 appears in a quite narrow P-T window ranging from 0.60-0.85 GPa and 600-660°C (field labeled in bold in Fig. 6). The upper T limit is represented by the appearance of aluminosilicate (kyanite or sillimanite) whereas the upper P limit is determined by the formation of rutile; both phases are absent in the rock and, likely, were never part of the assemblage since no relicts are preserved. Compositional isopleths (Fig. 7) of garnet and matrix phases (Vance and Mahar, 1998) were used to obtain a P-T path (Fig. 8). The garnet core isopleths intersect at P ~ 0.5 GPa and T ~ 550–560°C, (*c*. 25°C above the garnet-in curve). This intersection is in a field with chlorite present and plagioclase absent (Fig. 8), in agreement with the inclusion mineral assemblage in the garnet core. According to the trend of chemical zoning in garnet (Fig. 5a, b; Fig. 7), the prograde evolution of KL-19 must be characterized by both increasing P and T along a clockwise P-T path (see also Vance and Mahar, 1998). The peak P never reached pressures of the rutile-in curve. A later stage of slight decompression from nearly 0.8 GPa (as suggested by Si^{4+} in white mica) up to 0.68 GPa and 640°C is suggested by the trend of the white mica composition, XMg in staurolite, as well as the chemical composition of the garnet rim. Equilibration at 0.68 GPa and 640°C is consistent with the result of the average P-T method of THERMOCALC (T = 634 ± 28°C, P = 0.67 ± 0.13 GPa, $a_{(H_2O)}$=1) applied to the garnet rim + average of rims of matrix phases (Fig. 8). This stage is also supported by Ti-in-biotite thermometry based on Henry et al. (2005) which returned T = 629 ± 15°C. These estimates are, within errors, in agreement with previous P-T results reported by Vannay and Hodges (1996) for metapelitic and garnet-bearing orthogneiss samples coming from the same structural position.

5. MONAZITE U-(Th)-Pb GEOCHRONOLOGY

5.1 Monazite Texture and Chemistry

In the two samples, orthogneiss KL-21 and paragneiss KL-19, monazite was dated in textural context (e.g. Williams and Jercinovic, 2002, 2012) to add time constraints to the P-T evolution of the KSZ. Monazite grains, their textural position and internal features (e.g. inclusions, zoning etc.) were characterized with a PHILIPS XL30 Scanning Electron Microscope at Università di Pisa. Multiple point analyses were computed on selected monazite grains with a JEOL 8200 Super probe at Earth Sciences Department of the University of Milan (Italy) following the analytical procedure as reported in Montomoli et al. (2013). Representative analyses of monazite grains are reported in Table 2.

Selected grains, representative of all the structural/chemical domains, were target for *in situ* geochronology with a laser-ablation, inductively coupled plasma mass spectrometer (LA-ICP-MS) using an Ar-F 193-nm excimer laser (GeoLas 102 from Micro-Las) at CNR-Istituto di Geoscienze e Georisorse at Pavia. Details on the full analytical procedure are reported in Paquette and Tiepolo (2007). Single analyses were performed by a one-minute acquisition of the background signal followed by recording, for at least 30 s, the ablation signal of the masses related to the isotopes ^{202}Hg, ^{204}(Hg + Pb), ^{206}Pb, ^{207}Pb, ^{208}Pb, ^{232}Th, and ^{238}U. The presence of common Pb was evaluated in each analysis on the basis of the net signal of ^{204}Pb (i.e. subtracted for the interference of ^{204}Hg and background). None of the sample revealed ^{204}Pb counts above the background level. However, the relatively high Hg signal in the gas blank does not exclude the effective presence of common Pb in the analysed monazite. Laser-induced elemental fractionation and mass bias were corrected using matrix-matched external monazite standard (Moacir monazite: Cruz et al., 1996; Seydoux-Guillaume et al., 2002a, b) and considering the values, re-calibrated for isotopic disequilibrium, reported by Gasquet et al. (2010); the relative standard deviation of the analyses is mostly within 2-4 %. Monazite ages are plotted on the U-Th-Pb concordia (Fig. 10) as suggested by Foster et al. (2000; see also Stearns et al., 2013) and interpreted according to their chemistry and textural positions. Data processing and plotting was done with the software ISOPLOT (Ludwig, 2003). Isotopic results and calculated ages are reported in Table 3.

A sub population of monazite crystals were analysed by ion microprobe. Portions of thin sections were mounted in epoxy resin with a polished standard block. Backscattered electron (BSE) images for monazite were carried out on a JEOL JSM_6610A scanning electron microscope (SEM) at the Australian National University (ANU) in Canberra. Operating conditions for the SEM were 15 kV/60 µA and 20 mm working distance. Imaging revealed that most crystals in either sample are homogeneous in BSE; others have small, bright cores.

Monazite was analysed for U, Th and Pb isotopes using the sensitive high resolution ion microprobe SHRIMP-II at the ANU. Instrumental conditions and data acquisition were generally as described by Williams (1998) and energy filtering was applied to remove interferences and reduce matrix effects as described in Rubatto et al. (2001). The measured ^{206}Pb/^{238}U ratio was corrected using reference monazite USGS44069 (425 Ma, Aleinikoff et al., 2007). The analyses were corrected for common Pb based on the measured ^{204}Pb and ^{207}Pb/^{206}Pb according to the method described in Williams (1998). The analytical session had a calibration error of 2.5% (2 sigma), which was propagated to single analyses. The percent of common Pb in each analysis varied between 0.2 and 2.4% and the common Pb composition was assumed to be that predicted by the model of Stacey and Kramers (1975). Data evaluation and age calculation were done using the software Squid 1 and Isoplot/Ex (Ludwig 2003), respectively. The ion microprobe set up is not suited to accurately measure the high Th signal in monazite and thus ^{206}Pb/^{238}U ages are preferred because they are more accurate and precise. The agreement of SHRIMP ^{206}Pb/^{238}U and LA-ICP-MS ^{208}Pb/^{232}Th ages for unzoned monazite crystals indicates that any excess ^{206}Pb from the decay of ^{230}Th is below analytical uncertainty of the calculated ages.

5.2 Texture and chemistry

Monazite crystals identified in thin sections in both samples are 25-150 µm in size. In orthogneiss KL-21 sample, subhedral to anhedral monazite grains are found along the mylonitic foliation, both in granoblastic and lepidoblastic layers. Monazite in the paragneiss KL-19 is euhedral to subhedral, commonly aligned to the foliation, with equilibrium crystal boundaries with other minerals. Some grains are included in garnet and one grain was found enclosed in staurolite. Other common accessory minerals in both samples are zircon, apatite and sporadic xenotime. Inclusions in monazite are quartz, mica, zircon and apatite in both samples. Rare tiny U-Th oxide grains are enclosed in monazite of the paragneiss.

The analysed monazites accommodate variable amounts of U and Th with a combination of cheralite and huttonite substitutions (Fig. 9a and b) as commonly observed in monazite (e.g. Spear and Pyle 2002). In KL-19, monazites included in garnet are enriched in HREE compared with matrix monazites (Fig. 9c). In the orthogneiss sample KL-21, monazite HREE composition is relatively tight and no clear monazite sub-population can be distinguished on the bases of its REE composition.

5.3 Results

LA-ICP-MS analyses of monazite from the two samples returned $^{208}Pb/^{232}Th$-$^{206}Pb/^{238}U$ concordant dates that span from about 27 to 48 Ma (Fig. 10, Table 3). Notably, the older three dates (~ 44, 46 and 49 Ma) were obtained from monazite included in the garnet rim of paragneiss KL-19 (Fig. 5, 10), whereas 13 analyses on monazite grains along the S_2 foliation gave younger dates (~ 30-42 Ma). Monazite grains along the main foliation in the orthogneiss (KL-21) provided dates in the range of ~ 27-41 Ma, which are similar to those obtained from monazite grains aligned along the S_2 foliation in the paragneiss. A monazite core from the orthogneiss yields a concordant date at 502±8.8 Ma (Table 3).

Monazite in the matrix of both samples analysed by SHRIMP yield dates that cover a large time span: in metapelite KL-19 from 28 to 46 Ma and in gneiss KL-21 from 33 to 41 Ma (Fig.11, Table 4), with most data in both samples in the range 34 to 41 Ma. There is no systematic correlation between Th and U content and age. Only two analyses could be located on the texturally older core rich in Th and in either samples these core analyses yield the oldest date at ~41 and 46 Ma.

Eight monazite grains were analysed both by LA-ICP-MS and SHRIMP: 6 grains in metapelite sample KL-19 and 3 grains in gneiss Kl-21 (Table 3 and 4). Because of the small size of the monazite grains and of their zoning (Fig. 10, 11), and the different sampling volume of the instruments (LA-ICPMS crater of 10 µm in diameter and about 8 µm in depth, SHRIMP crater of 20 µm in diameter and 2 µm depth) direct comparison between the results is not straightforward (Fig. 12).

A number of monazite grains from both samples show agreement between dates obtained by the two methods. Examples are KL-19 grain 317 from sample with $^{206}Pb/^{238}U$ ages of 40.5±0.6 Ma and 40.2±0.6 Ma by SHRIMP and 40.0±0.7 and 38.6±0.7 Ma by LA-ICP-MS; KL-21 grain 212 has a SHRIMP age of 38.4±0.6 Ma and a LA-ICP-MS age of 38.6±0.7 Ma (see also KL-19 grain 201). In these cases it can thus be concluded that the monazite grains are unzoned in age and the different volumes sampled make no difference on the measured date.

For other monazite grains the difference in age obtained with the two techniques and thus sampling volumes is significant. For example in KL-19 grains 308 and 307 three SHRIMP analyses are in the range 34.4 – 36.6 Ma whereas LA-ICP-MS gives dates ranging between 30.8±0.5 and 41.3±0.7 Ma. In another case from sample KL-21 grain 216 yielded SHRIMP dates of 40.7±0.6 in the Th-rich core and 32.8 to 35.4 Ma in the rim, whereas LA-ICPMS dates are closer together at 36.5±0.7 and 37.9±0.7 Ma. Similarly, in KL-19 grain 301 the SHRIMP date is older at 41.6±0.6 than the 34.4±0.6 Ma date by LA-ICP-MS. These discrepancies in measured date indicate that the small monazite grains are zoned in age – this age zoning correspond to chemical zoning only in some grains – and the different dating methods do not equally resolve and/or mix the distinct growth domains.

In the couple of grains where core-rim textures are evident, there is a good textural correspondence with older ages in cores and younger ages in rims (Fig. 12). Older monazite dates around 44-48 Ma are found in the grains included in garnet or cores of monazites along the foliation testifying the occurrence of older monazites reoriented and possibly partially re-equilibrated during the formation of S_2 foliation. The small size of the grains and the real possibility of mixing with younger rims make establishing the exact age of this older component arduous. In sample KL-19 the time span for the monazite rims varies from ~34 to 42 Ma. In sample KL-21 the rim dates are from ~32 to 39 Ma. The two samples show consistent ages indicating a prolonged monazite crystallization and recrystallization over nearly 10 Ma. Assigning the older monazite core ages to prograde metamorphism, the 10 Ma span is taken to indicate the development of the S_2 foliation.

6. DISCUSSION

Field observations (Fig. 2) and structural analysis at the meso- and micro-scale (Fig. 3-4) confirm the occurrence of a high-temperature contractional top-to-the-S/SW shear zone in the upper part of the GHS: the KSZ, localized close to the boundary between Unit 2 and Unit 3. The KSZ strikes NNW-ESE and crops out for several km from Kalopani to the SE (Fig. 2). Pseudosection modeling and inverse geothermobarometry (Fig. 6–8) highlighted that staurolite and garnet paragneisses (KL-19) involved in the shear zone record equilibration in the P-T range of 0.60-0.85 GPa and of 600-660°C (Fig. 8). This temperature range is in agreement with deformation temperatures suggested by quartz and feldspar microstructures.

The correlation between structural position of monazite (inclusions in garnet rim) and chemical zoning in garnet and monazite (Th-rich cores in matrix monazite) indicate that the older monazite at 48-41 Ma formed toward the end of prograde garnet growth, before development of the S_2 foliation. In Fig. 5 the monazite at 48-41 Ma marks the changing in zoning of garnet. We attribute the formation of monazite in the matrix of KL-19 garnet-staurolite-bearing paragneiss over the period ~41-28 Ma to the decompression path and development of S_2 foliation during the shearing of the Kalopani shear zone. Orthogneiss KL-21 does not contain garnet, and monazite ages in this sample are in the range 41-32 Ma (with the exclusion of discordant analyses and an outlier at 27 Ma). One single monazite core was dated at ~ 41 Ma. We thus suggest that in this sample prograde monazite, was nearly completely reset during development of the S_2 foliation because it was not shielded by garnet. One concordant age at 502 Ma (Fig. 10) in sample KL-21 is interpreted as the age of the magmatic protolith, in agreement with Godin et al. (2001).

White micas along S_2 and the outermost garnet rim mark the beginning of decreasing pressure (Fig. 8) and consequently the start of exhumation of the studied part of the GHS. The lacking of strain shadows or tails along monazite, and the equilibrium grain boundaries, along S_2 foliation reinforce the interpretation that the monazite growth occurred during the growth of other S_2 minerals.

The initial exhumation of the uppermost part of the GHS (*i.e.* hanging wall of the KSZ) was triggered by the activity of the Kalopani contractional shear zone. Our data point to exhumation from ~41 Ma, which is the oldest record within the GHS. This event would be even older than exhumation at ~26 Ma induced by the HHD in the lower-middle part of the GHS (Montomoli et al., 2013, 2015; Iaccarino et al., 2015).

The suggested early exhumation of the GHS is in agreement with the drastic change of sediments provenance in the Himalayan foredeep starting from Middle Eocene (Najman and Garzanti, 2000) and with the occurrence of detritus coming from crystalline rocks in the Bengal fan starting from 39 Ma (Najman et al., 2008). This testifies that, by that time, exhumation brought GHS crystalline rocks up to the surface during an early evolution of the Himalaya.

Ages as old as 48-44 Ma have been reported by Carosi et al., (2010) and Larson and Cottle (2015) from monazite included in garnet and as isolated ages from garnet-kyanite bearing paragneisses from Lower Dolpo (Western Nepal) and kyanite-bearing veins/leucosomes in the Kali Gandaki valley belonging to Unit 1 of the GHS. Scattered monazite dates as old as Early Eocene (45 and 48 Ma) related to prograde metamorphism and a contractional shear zone (KSZ) allow to speculate a metamorphic and tectonic setting related to early crustal thickening in frontal parts of the belt at that time. The activity of the KSZ at c. 41-30 Ma testifies an action of contractional tectonics affecting the northern margin of India, now incorporated in the main Himalayan range.

6.2. Geodynamic implications

The HHD in the Kali Gandaki valley with ages from ~25 to 18 Ma (monazite U-Th-Pb ages, Iaccarino et al., 2015), has been recently identified close to the base of the kyanite-bearing gneiss in Unit 1 (Fig. 1b). We propose that, at the time of activation of the HHD, both the hanging- and foot-wall of the KSZ (now included as hanging wall of the HHD) were exhumed (Fig. 13). Only when deformation shifted to the MCT zone, the entire GHS underwent exhumation and then retrogression.

The new data can be reconciled with a three stage exhumation of the GHS starting from ~ 41 Ma and driven by the progressive activation of contractional top-to-the-SW shear zones (Fig. 13). He et al. (2015) proposed a similar three stage exhumation in the GHS by thrusts 1, 2 and 3 progressively activated towards the foreland during the Oligocene with the oldest thrust being active at ~ 26 Ma. Slices of the Indian continental margin have been progressively incorporated in the orogen. However, following the model proposed by of He et al. (2015), we argue that a difference in the timing of prograde metamorphism, or at least a part of it, is expected for the three slices. A major difference is however in the timing of exhumation, which is progressively younger toward the foreland and is triggered by three major ductile contractional shear zones occurring within the GHS (Fig. 13). A consequence of this observation is that GHS underwent underthrusting below the Asian plate and progressive metamorphism and after some million years from the collision, slices of Indian crust were exhumed progressively, starting from the upper one.

The incorporation of the LHS in the belt is marked by P-T paths with significantly lower peak pressures and different shapes (hairpin P-T paths, e.g. Kohn et al., 2001, 2008; Rolfo et al., 2015). Subsequently, additional slices of the LHS were incorporated in the crustal wedge recording progressively lower P-T values and activating a duplexing mechanism (Robinson and Martin, 2014).

Exhumation starting from ~ 41 Ma in shear zones at the higher level of the GHS with respect to the MCT does not support previous exhumation models in which the exhumation is mainly driven by the coupled activities of the STDS and MCT at 23-17 Ma with opposite kinematics. Such models are: rigid and ductile extrusion, channel flow, channel flow followed by extrusion and wedge insertion (see Montomoli et al., 2013 for an overview of the models). The activity of the STD and/or erosion and kinematic thinning of the GHS (or combination of these) could explain the exhumation process based on the activity of contractional shear zones. Even if in principle an older channel flow could be localized in the uppermost part of the GHS, as already pointed out by Montomoli et al. (2013; see also He et al., 2015) there is not enough thickness of the GHS above the HHD to generate a “large scale” channel flow (as the models require a 10-20 km thick GHS; Beaumont et al., 2001) and even less space is available for the relatively thin hanging-wall of the KSZ delimitated to the North by the Annapurna Detachment (the local strand of the STDS in the Kali Gandaki; Searle, 2010).

Prograde metamorphism at this stage was limited to the lower GHS, which continued to be underthrust beneath the HHD. The Bura Buri leucogranite intruded at 23-24 Ma across the STD and locked the contact between GHS and TSS (Carosi et al., 2013) in western and central (?) Nepal. The intrusion of the Mugu granite or similar granitic bodies occurred later at ~ 19 Ma (Harrison et al., 1999).

In the time span 17-13 Ma in Western Nepal (Montomoli et al, 2013), 22-16 Ma in Central Nepal (Catlos et al., 2001) and 17-11 Ma in Sikkim (Anczkiewicz et al., 2014), the MCT zone became active resulting in the overall exhumation of the GHS. At this stage, the metamorphism was shifted to the Lesser Himalayan Sequence becoming involved in the deformation propagating to the South (Mottram et al., 2014).

In this framework, the P-T-t paths of the slices of the GHS, delimited by the top-to-the-SW shear zones, are of similar shape. However, they are diachronous because the slices were initially underthrust to the NE, but exhumed at different times coinciding with the activation of the shear zone underneath the exhumed slice (Montomoli et al., 2013, 2015). The timing of exhumation shows a difference of several million years between the hanging-wall and footwall of the HHD (*e.g.* 5-6 Ma, Montomoli et al., 2013, 2015).

The diachronous activation of contractional top-to-the-S and SW shear zones within the GHS, while it experienced an overall underthrusting, explains the relatively low peak P recorded by the hanging-wall compared to that of the footwall rocks (Carosi et al., 2010). The difference in pressure (at peak temperature) from literature data is estimated to be at least 0.2-0.3 GPa (Kohn, 2008; Montomoli et al., 2013, 2015). In this framework older ages (up to ~ 25 Ma) are found in the upper portion of the GHS as already pointed out by previous workers (Kohn et al. 2005; Corrie and Kohn 2011; Kohn 2008, 2014, 2016; Montomoli et al., 2013; Ambrose et al. 2015; Wang et al., 2015). A similar mechanism of propagation of shear zones toward the foreland has been proposed by Ambrose et al. (2015) who combined monazite geochronology and pseudosection modeling to identify the sequence of activation of shear zones. They propose the occurrence of several "cryptic" shear zones and "ductile" thrust sheets progressively activated at 24-18 Ma in the mid crust (GHS) of Eastern Nepal. Ambrose et al. (2015) in sequence-thrusting model implies that external ductile "duplexes" in the mid crust underwent still prograde metamorphism when the hanging-wall was exhumed, as also proposed by Montomoli et al. (2013). Crustal slices are progressively incorporated from the footwall in the southward propagating orogenic wedge. However the available data from the timing of prograde metamorphism in the lower part of the GHS point to a prograde metamorphism of the kyanite-bearing gneiss at 43-36 Ma in the Kali Gandaki valley (Carosi et al., 2015; Iaccarino et al., 2015) before the activation of the propagation of shear zones at

24-18 Ma, and consequent exhumation of the hanging-wall and prograde metamorphism in the footwall, as proposed by Ambrose et al. (2015) and Larson et al. (2015).

6.3 Folded Isograds in the GHS

Occurrence of Barrovian index minerals such as garnet, staurolite and kyanite both in the upper and in the lower part of the GHS (i.e. in the MCT zone) has been often regarded as an evidence of large-et al., 2008; Searle, 2010). Geochronological data on staurolite-bearing paragneiss (sample KL-19) localized in the uppermost portion of the GHS offer the opportunity to check if Barrovian metamorphism is contemporaneous in the upper and in the lower portions of the GHS. Barrovian index minerals, e.g. garnet, can grow during different P-T trajectories (related to different tectonic settings) and record different stages of metamorphism during their growth (e.g. Spear et al., 1990; Caddick and Kohn, 2013). In addition, bulk rock compositions play an important role in the development of Barrovian index minerals (e.g. Spear 1993). Therefore we prefer to compare if during the same time span rocks from the upper and lower GHS recorded the same prograde, decompressional and/or retrograde paths.

In the upper part of the GHS in the study area, monazite geochronology is compatible with a retrograde path at 41-30 Ma (samples KL-21 and KL-19, this work). In the lower part of the GHS garnet and kyanite show prograde growth from (at least) 43-36 Ma and a retrograde one at 25-18 Ma (samples K-28a and c in Carosi et al., 2015 and Iaccarino et al., 2015 respectively). The Barrovian minerals thus grew in different periods of time. Moreover, retrograde segments of the P-T paths are shifted by several million years from the upper to the lower part of the GHS (see also Kohn, 2014). This finding does not support the hypothesis of folded Barrovian isograds or passively folded isograds by the southward motion of the hot-channel made of partially molten rocks (Searle and Szulc, 2005; Jessup et al., 2008; Searle, 2010). Moreover, according to this work and Iaccarino et al. (2015) Barrovian minerals in the upper and lower part of the GHS were not part of the same tectonic units because the GHS has been effectively subdivided in three tectonic units bounded by the KSZ, HHD and MCT.

Another aspect that is worth considering is the age of the main foliation in the GHS. According to the channel-flow model the foliation should be developed at the same time all over the GHS during the horizontal motion along the hot-channel between 23 and 17 Ma (Grujic, 2006). Our new age data on the development of the foliation in the sheared uppermost part of the GHS at 41-30 Ma, is older with respect to the age of the foliation in the HHD (25-18 Ma) and in the MCT zone (younger than 17-18 Ma). Similar differences in age between upper and lower GHS have been reported by Imayama et al. (2012) and Rubatto et al. (2013) in Sikkim and Wang et al. (2015) in Central Nepal. This timing does not support the hypothesis of a foliation developed in the same time span in a tectonic unit being as thick as 10-20 km as requested by the channel flow model (Beaumont et al., 2001; Grujic, 2006).

7. CONCLUSIONS

The kinematics of ductile shear zones, P-T paths and monazite U-Th-Pb ages recorded within the GHS highlight that exhumation occurred at ~ 41-30 Ma and did not affect the entire GHS at the same time. The high-temperature KSZ in the upper part of the GHS triggered the earlier exhumation of this sequence.

Taking into consideration recently published age data on the activity of the HHD and MCT, it is evident that the exhumation process, firstly localized in the hanging-wall of the uppermost shear zone shifted downwards and resulted in progressively larger portions of the GHS being exhumed. When deformation was finally localized along the MCT, the entire GHS underwent exhumation. It is noteworthy that three different GHS slices (or sub-units) separated by the KSZ, HHD and MCT underwent diachronous metamorphism reaching peak T and P at different times and showing younger ages of exhumation progressively moving structurally downward in the orogenic pile (Fig. 13).

Middle – Late Eocene exhumation of the upper part of the GHS cannot be explained by the contemporaneous activity of MCT and STD, which occurred later, and by previously published exhumation models such as the extrusion, wedge insertion, channel flow and channel flow followed by extrusion models. A model that takes into account the occurrence of tectonic and metamorphic discontinuities in the upper GHS, which progressively shifted to the lower part of the GHS and later into the LHS, is able to explain the newly obtained data.

ACKNOWLEDGEMENTS

We are grateful to T. Theye (Universität Stuttgart) for the help with electron microprobe analysis. The research was supported by PRIN 2010–2011 to R. C. and C. M. and local research funds from Torino and Pisa Universities.

REFERENCES

Ambrose, T.K., Larson, K.P., Guilmette, C., Cottle, J.M., Buckingham, H., and Rai. S., 2015, Lateral extrusion, underplating, and out-of-sequence thrusting within the Himalayan metamorphic core, Kanchenjunga, Nepal: Lithosphere, v. 7, p. 441–464, doi:10.1130/L437.1.

Anczkiewicz, R., Chakraborty, S., Dasgupta S., Mukhopadhyay, D., and Kołtonik, K., 2014, Timing, duration and inversion of prograde Barrovian metamorphism constrained by high resolution Lu–Hf garnet dating: A case study from the Sikkim Himalaya, NE India, Earth and Planetary Science Letters, v. 407, p. 70–81, doi:10.1016/j.epsl.2014.09.035.

Antolín, B., Appel, A., Montomoli, C., Dunkl, I., Ding, L., Gloaguen, R., and El Bay, R., 2011, Kinematic evolution of the eastern Tethyan Himalaya: constraints from magnetic fabric and structural properties of the Triassic flysch in SE Tibet, *in* Poblet, J., Lisle, R., eds., Kinematic Evolution and Structural Styles of Fold-and-Thrust Belts: Geological Society of London Special Publications 349, p 99–121. http://dx.doi.org/10.1144/SP349.6.

Beaumont, C., Jamieson, R.A., Nguyen, M.H. and Lee, B., 2001, Himalayan tectonics explained by extrusion of a low-viscosity crustal channel coupled to focused surface denudation: Nature, v. 414, p. 738–742, doi:10.1038/414738a.

Bertoldi, L., Massironi, M., Visonà, D., Carosi, R., Montomoli, C., Gubert, F., Naletto, G. and Pelizzo, M.G., 2011, Mapping the Buraburi granite in the Himalaya of Western Nepal. Remote sensing analysis in a collisional belt with vegetation cover and estreme variation of topography: Remote Sensing of Environment, v. 115, p. 1129–1144, doi:10.1016/j.rse.2010.12.016.

Bordet, P., Colchen, M., Krummenacher, D., Le Fort, P., Mouterde, R., and Remy, M., 1971, Recherches géologiques dans l' Himalaya du Nepal, region de la Thakkhola C.N.R.S, Paris (1971) 279 pp.

Brown, R.L., and Nazarchuk, J.H., 1993, Annapurna detachment fault in the Greater Himalaya of central Nepal, *in* Trelor, P.J and Searle, M.P., eds., Himalayan Tectonics, Geological Society of London Special Publications 74, p. 461–473, doi:10.1144/GSL.SP.1993.074.01.31.

Burchfiel, B.C., Chen, Z., Hodges, K.V., Liu Y., Royden, L.H., Changrong, D., and Xu, L., 1992, The South Tibetan Detachment System, Himalayan Orogen: Extension contemporaneous with and parallel to shortening in a collisional mountain belt: Geological Society of America

Special Paper, v. 269, p. 1–41, doi:10.1130/SPE269-p1.

Burg, J.P., Brunel, M., Gapais, D., Chen, G.M., and Liu, G.H., 1984, Deformation of leucogranites of the crystalline Main Central Sheet in southern Tibet (China): Journal of Structural Geology, v. 6, p. 535–542, doi:10.1016/0191-8141(84)90063-4.

Caby, R., Pêcher, A., and Le Fort, P., 1983, Le grand chevauchement central himalayen: Nouvelles données sur le métamorphisme inverse à la base de la Dalle du Tibet. Revue de Géologie Dynamique et de Géographie Physique v. 24, p. 89–100.

Caddick, M.J., and Kohn M.J., 2013, Garnet as a monitor of the conditions in the evolving crust and lithosphere: Elements, v. 9, p. 427-432, doi:10.2113/gselements.9.6.427.

Carosi, R., Lombardo, B., Molli, G., Musumeci, G., and Pertusati, P.C., 1998, The South Tibetan detachment system in the Rongbuk valley, Everest Region. Deformation features and geological implication: Journal of Asian Earth Sciences, v. 16, p. 299–311, doi:10.1016/S0743-9547(98)00014-2.

Carosi, R., Lombardo, B., Musumeci, G., and Pertusati, P.C., 1999, Geology of the Higher Himalayan Crystallines in Khumbu Himal (Eastern Nepal): Journal of Asian Earth Science, v. 17, p. 785–803, doi:10.1016/S1367-9120(99)00014-0.

Carosi, R., Montomoli, C., Visonà, D., 2002. Is there any detachment in the Lower Dolpo (western Nepal)?: Comptes Rendus Geoscience, v. 334, p. 933-940, doi:10.1016/S1631-0713(02)01828-X.

Carosi, R., Montomoli, C., and Visonà, D., 2007, A structural transect in the Lower Dolpo: Insights on the tectonic evolution of Western Nepal: Journal of Asian Earth Science, v. 29, p. 407–423, doi: 10.1016/j.jseaes.2006.05.001.

Carosi, R., Montomoli, C., Rubatto, D., and Visonà D., 2010, Late Oligocene high-temperature shear zones in the core of the Higher Himalayan Crystallines (Lower Dolpo, Western Nepal): Tectonics, v. 29, TC4029, doi:10.1029/2008TC002400.

Carosi, R., Montomoli, C., Rubatto, D., and Visonà D., 2013, Leucogranite intruding the South Tibetan Detachment in western Nepal: implications for exhumation models in the Himalayas: Terra Nova, v. 25, p. 478-489, doi:0.1111/ter.12062.

Carosi, R., Montomoli, C., Langone, A., Turina, A., Cesare, B., Iaccarino, S., Fascioli, L., Visonà, D., Ronchi, A., and Santa Man, R., 2015, Eocene partial melting recorded in peritectic garnets from kyanite-gneiss, Greater Himalayan Sequence, central Nepal, *in* Mukherjee, S., Carosi, R., van der Beek, P.A., Mukherjee, B.K., Robinson, D.M., eds., Tectonics of the Himalaya: Geological Society, London, Special Publications 412, p. 111–129, First published online September 9, 2014, doi:10.1144/SP412.1.

Carosi, R., Gemignani, R., Godin, L., Iaccarino, S., Larson, K., Montomoli, C., and Rai, S., 2014, A geological journey through the deepest gorge on Earth: the Kali Gandaki valley section, central Nepal, *in*: Montomoli, C., Carosi, R., Law, R., Singh, S., Rai, S.M., eds., Geological field trips in the Himalaya, Karakoram and Tibet, Journal of the Virtual Explorer, Electronic Edition, ISSN 1441-8142, v. 47, paper 9, doi:10.3809/jvirtex.2014.00337.

Catlos E.J., Harrison, T.M., Kohn, M.J., Grove, M., Ryerson, F.J., Manning, C.E., and Upreti, B.N., 2001, Geochronologic and thermobarometric constraints on the evolution of the Main Central Thrust, central Nepal Himalaya: Journal of Geophysical Research, v. 106, p. 16,177–16,204, doi: 10.1029/2000JB900375.

Catlos E.J., Harrison, T.M., Manning, C.E., Grove, M., Rai, S., Hubbard, M.S., and Upreti, B.N., 2002, Records of the evolution of the Himalayan orogen from in situ Th–Pb ion microprobe dating of monazite: Eastern Nepal and western Garhwal: Journal of Asian Earth Sciences, v. 50, p. 459–479, doi:10.1016/S1367-9120(01)00039-6.

Colchen, M., Le Fort, P., and Pêcher, A., 1986, Notice explicative de la carte géologique Annapurna–Manaslu–Ganesh (Himalaya du Népal) au 1:200 000e (bilingual: French–English), CNRS, Paris, 1986.

Connolly, J.A.D., 2005, Computation of phase equilibria by linear programming: A tool for geodynamic modelling and its application to subduction zone decarbonation: Earth and Planetary Science Letters, v. 129, p. 524-541, doi:0.1016/j.epsl.2005.04.033.

Corrie, S.L., and Kohn, M.J., 2011, Metamorphic history of the Central Himalaya, Annapurna region, Nepal, and implication for tectonic models: Geological Society of American Bulletin, v. 123, p. 1863–1879, doi:10.1130/B30376.1.

Cottle, J.M., Larson, K.P., and Kellett, D.A., 2015, How Does the Mid-crust Accommodate Deformation in Large, Hot Collisional Orogens? A review of recent research in the Himalayan Orogen: Journal of Structural Geology, v. 78, p. 119–133, doi:10.1016/j.jsg.2015.06.008.

Crouzet, C., Dunkl, I., Paudel, L., Arkai, P., Rainer, T.M., Balogh, K., and Appel E., 2007, Temperature and age constraints on the metamorphism of the Tethyan Himalaya in Central Nepal: A multidisciplinary approach: Journal of Asian Earth Sciences, v. 30, p. 113–130, doi:10.1016/j.jseaes.2006.07.014.

Cruz, M.J., Cunha, J.C., Merlet, C., and Sabaté, P., 1996, Dataçao pontual das monazitas da regiao de Itambé, Bahia, através da microssonda electrônica: XXXIX Congresso Brasileiro de Geologia, p. 206–209.

Daniel, C.G., Hollister, L., Parrish, R.R., and Grujic, D., 2003, Exhumation of the Main Central thrust from lower crustal depths, Eastern Bhutan Himalaya: Journal of Metamorphic Geology, v. 21, p. 317–334, doi:10.1046/j.1525-1314.2003.00445.x.

DeCelles, P.G., Gehrels, G.E., Quade, J., and Ojha, T.P., 1998, Eocene-early Miocene foreland basin development and the history of Himalayan thrusting, western and central Nepal: Tectonics, v. 17, p. 741–765, doi:10.1029/98TC02598.

Dunkl, I., Antolín, B., Wemmer, K., Rantitsch, G., Kienast, M., Montomoli, C., Ding, L., Carosi, R., Appel, E., El Bay, R., Xu, Q., and von Eynatten, H., 2011, Metamorphic evolution of the Tethyan Himalayan flysch in SE Tibet. *in* Gloaguen, R., Ratschbacher, L., eds., Growth and Collapse of the Tibetan Plateau: Geological Society of London Special Publications 353, 45–69, doi:http://dx.doi.org/10.1144/SP353.

Foster, G., Kinney, P., Vance, D., Prince, C., and Harris, N., 2000, The significance of monazite U-Th-Pb age data in metamorphic assemblages: A combined study of monazite and garnet chronometry: Earth and Planetary Science Letters, v. 181, p. 327-340, doi:10.1016/S0012-821X(00)00212-0.

Gansser, A., 1964, Geology of Himalayas. Wiley Interscience, London p. 289.

Gasquet, D., Bertrand, J.-M., Paquette, J.-L., Lehmann, J., Ratzov, G., De Ascençâo Guedes, R., Tiepolo, M., Boullier, A.-M., Scaillet, S., and Nomade, S., 2010, Miocene to Messinian deformation and hydrothermal activity in a pre-Alpine basement massif of the French western Alps: new U–Th–Pb and argon ages from Lauzière massif: Bulletin de la Société Géologique de France, v. 181, p. 227–241, doi:10.2113/ gssgfbull.181.3.227.

Gaetani, M., and Garzanti, E., 1991, Multicyclic History of the Northern India Continental Margin (Northwestern Himalaya): American Association of Petroleum Geologists Bulletin , v. 75, p.

1427–1446.

Godin, L., 2003, Structural evolution of the Tethyan sedimentary sequence in the Annapurna area, central Nepal Himalaya: Journal of Asian Earth Sciences, v. 22, p. 307-328, doi:10.1016/S1367-9120(03)00066-X.

Godin, L., Brown, R.L., and Hanmer, S., 1999, High strain zone in the hanging wall of the Annapurna detachment, central Nepal Himalaya, *in* Macfarlane, A., Sorkhabi, R.B., Quade, J., eds., Himalaya and Tibet: Mountain roots to mountain tops: Geological Society of America (Special Paper) 328, p. 199–210, doi:10.1130/0-8137-2328-0.199.

Godin, L., Parrish, R.R., Brown, R.L., and Hodges, K.V., 2001, Crustal thickening leading to exhumation of the Himalayan Metamorphic core of central Nepal: insight from U–Pb geochronology and $^{40}Ar/^{39}Ar$ thermochronology: Tectonics, v. 20, p. 729–747, doi:10.1029/2000TC001204.

Godin, L., Grujic, D., Law, R.D., and Searle M.P., 2006, Channel flow, ductile extrusion and exhumation in continental collision zones: an introduction, *in* Law, R.D., Searle, M.P., Godin, L., eds., Channel Flow, Ductile Extrusion and Exhumation in Continental Collision Zones: Geological Society of London Special Publication 268, p. 1-23, doi: 10.1144/GSL.SP.2006.268.01.01.

Groppo, C., Rolfo, F., and Lombardo, B., 2009, P–T Evolution across the Main Central Thrust Zone (Eastern Nepal): Hidden discontinuities revealed by petrology: Journal of Petrology, v. 50, p. 1149–1180, doi:10.1093/petrology/egp036.

Grujic, D., 2006, Channel Flow and continental collision tectonics: an overview, *in* Law, R.D., Searle, M.P., Godin, L., eds., Channel Flow, Ductile Extrusion and Exhumation in Continental Collision Zones: Geological Society of London Special Publication 268, p. 25–37, doi:10.1144/GSL.SP.2006.268.01.02.

Harrison, T.M., Grove, M., Lovera, O.M., Catlos, E.J., and D’Andrea, J., 1999, The origin of Himalayan anatexis and inverted metamorphism: Models and constraints: Journal of Asian Earth Sciences, v. 17, p. 755–772, doi:10.1016/S1367-9120(99)00018-8.

Herron, M.M., 1988, Geochemical classification of terrigenous sands and shales from core or log data: Journal of Sedimentary Research, v. 58, p 820-829, doi:10.1306/212F8E77-2B24-11D7-8648000102C1865D.

He, D., Webb, A.A., Larson, K.P., Martin, A.J., and Schmitt, A.K., 2015, Extrusion vs. duplexing models of Himalayan mountains building 3: duplexing dominates from the Oligocene to Present: International Geology Review, v. 57, p. 1–27, doi:10.1080/00206814.2014.986669.

Henry, D.J., Guidotti, C.V., and Thomson, J.A., 2005, The Ti-saturation surface for low-to-medium pressure metapelitic biotites: Implications for geothermometry and Ti-substitution mechanisms: American Mineralogist, v. 90, p. 316-328, doi: 10.2138/am.2005.1498.

Hodges, K.V., 2000, Tectonic of Himalaya and southern Tibet from two perspectives: Geological Society of America Bulletin, v. 112, p. 324-350, doi:10.1130/0016-7606(2000)112<324:TOTHAS>2.0.CO;2.

Hodges, K.V., Parrish, R.R., and Searle, M.P., 1996, Tectonic evolution of the Central Annapurna Range Nepalese Himalayas: Tectonics, v. 15, p. 1264-1291, doi: 10.1029/96TC01791

Hodges, K.V., Parrish, R.R., Housh, T.B., Lux, D.R., Burchfiel, B.C., Royden, L.H., and Chen, Z., 1992, Simultaneous Miocene extension and shortening in the Himalayan Orogen: Science, v. 258, p. 1466–1470.

Jessup, M.J., Cottle, M.J., Searle, M.P., Law, R.D., Newell, D.L., Tracy, R.J., and Waters, D.J., 2008, P–T–t–D paths of Everest Series schist, Nepal: Journal of Metamorphic Geology, v. 26, p. 717-739, doi: 10.1111/j.1525-1314.2008.00784.x.

Kellett, D., Grujic, D., and Erdmann, S., 2009, Miocene structural reorganization of the South Tibetan detachment, eastern Himalaya: Implications for continental collision: Lithosphere, v. 1, p. 259-281, doi:http://dx.doi.org/10.1130/L56.1.

Khanal, S., Robinson, D.M., Kohn, M.J., and Mandai, S., 2015, Evidence for a far-traveled thrust sheet in the Greater Himalayan thrust system, and an alternative model to building the Himalaya: Tectonics, v. 34, p. 31–52, doi:10.1002/2014TC003616.

Kohn, M.J., 2008, P-T-t data from Nepal support critical taper and repudiate large channel flow of the Greater Himalayan Sequence: Geological Society of America Bulletin, v. 120, p. 259–273, doi: 10.1130/B26252.1.

Kohn, M.J., 2014, Himalayan metamorphism and its tectonic implications: Annual Review of Earth and Planetary Sciences, v. 42, p. 381–419, doi:10.1146/annurev-earth-060313-055005.

Kohn, M.J., 2016, Metamorphic chronology comes of age: past achievements and future prospects: American Mineralogist, in press, doi:http://dx.doi.org/10.2138/am-2015-5146.

Kohn, M.J., Catlos, E., Ryerson, F.J., and Harrison, T.M., 2001, Pressure-Temperature-time path discontinuity in the Main Central thrust zone, Central Nepal: Geology, v. 29, p. 571-574, doi:10.1130/0091-7613(2001)029<0571:PTTPDI>2.0.CO;2.

Kohn, M.J., Wieland, M., Parkinson, C.D., and Upreti B.N., 2004, Miocene faulting at plate tectonic velocity in the Main Central thrust region, central Nepal: Earth and Planetary Science Letters, v. 228, p. 299-310, doi:10.1016/j.epsl.2004.10.007.

Kohn, M.J., Wielnand, M., Parkinson, C.D., and Upreti, B.N., 2005, Five generation of monazite in Langtang gneisses: implication for chronology of the Himalayan metamorphic core. Journal of Metamorphic Geology, v. 23, p. 399–406, doi:10.1111/j.1525-1314.2005.00584.x.

Iaccarino, S., Montomoli, C., Carosi, R., Massonne, H.-J., Langone, A. and Visonà D., 2015, Pressure–temperature–time–deformation path of kyanite-bearing migmatitic paragneiss in the Kali Gandaki valley (Central Nepal): Investigation of Late Eocene–Early Oligocene melting processes: Lithos, v. 231, p. 103-121, doi:10.1016/j.lithos.2015.06.005.

Imayama, T., Takeshite, T., Yi, K., Cho, D.-Y., Kitajima, K., Tsutsumi, Y., Kayama, M., Nishido, H., Okumura, T., Yagi, K., Itaya, T., and Sano, Y., 2012, Two-stage partial melting and contrasting cooling history within the Higher Himalayan Crystalline Sequence in the far-eastern Nepal Himalaya: Lithos, v. 134–135, p 1–22, doi: 10.1016/j.lithos.2011.12.004.

Larson, K.P., and Cottle, M.J., 2015, Initiation of crustal shortening in the Himalaya: Terra Nova, v. 27, p. 169–174, doi:10.1111/ter.12145.

Larson, K.P., Godin, L, and Price, R.A., 2010, Relationships between displacement and distortion in orogens: linking the Himalayan foreland and hinterland in central Nepal: Geological Society of American Bulletin, v. 122, p. 1116-1134, doi: 10.1130/B30073.1.

Larson, K.P., Gervais, F., and Kellett, D.A, 2013, A P-T-t-D discontinuity in east-central Nepal: Implications for the evolution of the Himalayan mid-crust: Lithos, v. 179, p. 275–292, doi:10.1016/j.lithos.2013.08.012.

Larson, K.P., Ambrose, T.K., Webb, A.A.G., Cottle, J.M., and Shrestha, S., 2015, Reconciling Himalayan midcrustal discontinuities: The Main Central thrust system: Earth and Planetary Science Letters, v. 429, p. 139–146, doi:10.1016/j.epsl.2015.07.070.

Law, R.D., Searle, M.P., and Simpson, R.L., 2004, Strain, deformation temperatures and vorticity of flow at the top of the Greater Himalayan Slab, Everest Massif, Tibet: Journal of Geological Society, v. 161, p. 305–320, doi:10.1144/0016-764903-047.

Le Fort, P., 1975, Himalaya: the collided range. Present Knowledge of the Continental Arc: American Journal of Science, v. 275, p. 1–44.

Linthout, K., 2007, Tripartite division of the system $2REEPO_4$–$CaTh(PO_4)_2$–$2ThSiO_4$, discreditation of brabantite, and recognition of cheralite as the name for members dominated $CaTh(PO_4)_2$: The Canadian Mineralogist, v. 45, p. 503–508, doi:10.2113/gscanmin.45.3.503.

Lombardo, B., Pertusati, P., and Borghi, S., 1993, Geology and tectonomagmatic evolution of the eastern Himalaya along the Chomolungma-Makalu transect, *in* Trelor, P.J and Searle, M.P., eds., Himalayan Tectonics, Geological Society of London Special Publications 74, p. 341–355, doi:10.1144/GSL.SP.1993.074.01.23.

Ludwig, K.R., 2003, Isoplot/Ex version 3.0 A geochronological toolkit for Microsoft Excel. Berkeley Geochronology Center, Special Publications, 4.

Massonne, H.-J., 2012, Formation of amphibole and clinozoisite-epidote in eclogite owing to fluid infiltration during exhumation in a subduction channel: Journal of Petrology, v. 53, p. 1969–1998, doi:10.1093/petrology/egs040.

Montomoli, C., Iaccarino, S., Carosi, R., Langone, A., and Visonà, D., 2013, Tectonometamorphic discontinuities within the Greater Himalayan Sequence in Western Nepal (Central Himalaya): Insights on the exhumation of crystalline rocks: Tectonophysics, v. 608, p. 1349–1370, doi:10.1016/j.tecto.2013.06.006.

Montomoli, C., Iaccarino, S., Antolin, B., Appel, E., Carosi, R., Dunkl, I., Ding, L., and Visonà,D., Tectono-metamorphic evolution of the Tethyan Sedimentary Sequence (Himalayas, SE Tibet). Italian Journal of Geosciences, in press.

Montomoli, C., Carosi, R., and Iaccarino, S., 2015, Tectonometamorphic discontinuities in the Greater Himalayan Sequence: a local or a regional feature? *in* Mukherjee, S., Carosi, R., van der Beek, P.A., Mukherjee, B.K., Robinson, D.M., eds., Tectonics of the Himalaya. Geological Society, London, Special Publications 412, p. 25–41. First published online September 18, 2014, doi:http://dx.doi.org/10.1144/SP412.3.

Mottram, C.M., Warren, C.J., Regis, D., Roberts, N.M.W., Harris, N.B.W., Argles, T.W., and Parrish, R.R., 2014, Developing an inverted Barrovian sequence; insights from monazite petrochronology: Earth and Planetary Science Letters, v. 403, p. 418–431, doi:10.1016/j.epsl.2014.07.006.

Mukherjee, S., Koyi, H.A., and Talbot, C., 2012, Implications of channel flow analogue models for extrusion of the Higher Himalayan Shear Zone with special reference to the out-of-sequence thrusting: International Journal of Earth Science (Geol. Rundsch.), v. 101, p. 253–272, doi:10.1007/s00531-011-0650-6.

Najman, Y., and Garzanti, E., 2000, Reconstructing early Himalayan tectonic evolution and paleogeography from Tertiary foreland basin sedimentary rocks, northern India: Geological Society of America Bulletin, v. 112, p. 435–449, doi:10.1130/0016-7606(2000)112<435:REHTEA>2.0.CO;2.

Najman, Y., Apple, E., Boudagher-Fadel, M., Bown, P., Carter, A., Garzanti, E., Godin, L., Han, J., Liebke, U., Oliver, G., Parrish, R., and Vezzoli, G., 2010, Timing of India-Asia collision: Geological, biostratigraphic, and palaeomagnetic constraints: Journal of Geophysical Research: Solid Earth, v. 115, doi:10.1029/2010JB007673.

Najman, Y., Bickle, M., BouDagher-Fadel, M., Carter A., Garzanti, E., Paul, M., Wijbrans, J., Willett E., Oliver, G., Parrish, R.R., Akhter S.H., Allen, R., Ando S., Chisty, E., Reisberg, L., and Vezzoli, G., 2008, The Paleogene record of Himalayan erosion: Bengal Basin, Bangladesh: Earth and Planetary Science Letters, v. 273, p. 1–14, doi:10.1016/j.epsl.2008.04.028.

Paquette, J.L., and Tiepolo, M., 2007, High resolution (5 μm) U-Th-Pb isotope dating of monazite with excimer laser ablation (ELA)-ICPMS: Chemical Geology, v. 240, p. 222–237, doi:10.1016/j.chemgeo.2007.02.014.

Passchier, C.W., Trouw, R.A.J., 2005. Microtectonics. Springer Verlag, pp. 366.

Pognante, U., Castelli, D., Benna, P., Genovese, G., Oberli, F., Meier, M., and Tonarini, S., 1990, The crystalline units of the High Himalayas in the Lahul–Zanskar region (northwest India): metamorphic–tectonic history and geochronology of the collided and imbricated Indian plate: Geological Magazine, v. 127, p. 101–116, doi:http://dx.doi.org/10.1017/S0016756800013807.

Powell, R., and Holland, T.J.B., 1994, Optimal geothermometry and geobarometry: American Mineralogist, v. 79, p. 120-133.

Robinson, D.M., and Martin, A.J., 2014, Reconstructing the Greater Indian margin: A balanced cross section in central Nepal focusing on the Lesser Himalayan duplex: Tectonics, v. 33, p. 2143–2168, doi:10.1002/2014TC003564.

Rolfo, F., Groppo, C., and Mosca, P., 2015, Petrological constraints of the 'Channel Flow' model in eastern Nepal, *in* Mukherjee, S., Carosi, R., van der Beek, P.A., Mukherjee, B.K., Robinson, D.M., eds., Tectonics of the Himalaya. Geological Society, London, Special Publications 412, p. 177–197. First published online September 9, 2014, doi:10.1144/SP412.4.

Rubatto, D., Chakraborty, S., and Dasgupta, S., 2013, Timescale of crustal melting in the Higher Himalayan Crystallines (Sikkim, Eastern Himalaya) inferred from trace element-constrained monazite and zircon chronology: Contribution to Mineralogy and Petrology, v. 165, p. 349-372, doi:10.1007/s00410-012-0812-y.

Schelling, D., 1992, The tectonostratigraphy and structure of the eastern Nepal Himalaya: Tectonics, v. 11, p. 925–943, doi:10.1029/92TC00213.

Searle, M.P., 1999, Extensional and compressional faults in the Everest–Lhotse Massif, Khumbu Himalaya, Nepal: Journal of the Geological Society of London 156, 227–240, doi:10.1144/gsjgs.156.2.0227.

Searle, M.P., 2010, Low-angle normal faults in the compressional Himalayan orogen; Evidence from the Annapurna–Dhaulagiri Himalaya, Nepal: Geosphere, v. 6, p. 296–315, doi:10.1130/GES00549.1.

Searle, M.P., and Godin, L., 2003, The South Tibetan Detachment System and the Manaslu Leucogranite: a structural reinterpretation and restoration of the Annapurna–Manaslu Himalaya, Nepal: Journal of Geology, v. 111, p. 505–523, doi:10.1086/376763.

Searle, M.P., Law, R.D., Godin, L., Larson, K.P., Streule, M.J., Cottle, M.J., and Jessup, M.J., 2008, Defining the Himalayan Main Central Thrust in Nepal: Journal of Geological Society, v. 165, p. 523–534, doi:10.1144/0016-76492007-081.

Searle, M.P., and Szulc, A.G., 2005, Channel flow and ductile extrusion of the high Himalayan slab-the Kangchenjunga–Darjeeling profile, Sikkim Himalaya: Journal of Asian Earth Sciences, v. 25, p. 173–185, doi:10.1016/j.jseaes.2004.03.004.

Seydoux-Guillaume, A.M., Paquette, J.L., Wiedenbeck, M., Montel, J.M., and Heinrich, W., 2002a, Experimental resetting of the U–Th–Pb systems in monazite: Chemical Geology, v. 191, p. 165–181, doi:10.1016/S0009-2541(02)00155-9.

Seydoux-Guillaume, A.M., Wirth, R., Nasdala, L., Gottschalk, M., Montel, J.M., and Heinrich, W., 2002b, An XRD, TEM and Raman study of experimentally annealed natural monazite: Physics and Chemistry of Minerals, v. 29, p. 240–253, doi: 10.1007/s00269-001-0232-4.

Stearns M.A., Hacker, B.R., Ratschbacher, L., Lee, J., Cottle, M.J., and Kylander-Clarc A., 2013, Synchronous Oligocene-Miocene metamorphism of the Pamir and the north Himalaya driven by plate scale dynamics: Geology, v. 41, p. 1071–1074, doi:10.1130/G34451.1.

Stephenson, B.J., Searle, M.P., Waters, D.J., and Rex D.C., 2001, Structure of the Main Central Thrust zone and extrusion of the High Himalayan deep crustal wedge, Kishtwar–Zanskar Himalaya: Journal of the Geological Society, v. 158, p. 637–652, doi:10.1144/jgs.158.4.637.

Spear, F.S., 1993, Metamorphic phase equilibria and pressure-temperature-time paths. Mineralogical Society of America, Monograph Series, Washington, D. C.

Spear, F.S., Kohn, M.J., Florence, F.P., and Menard, T., 1990, A model for garnet and plagioclase growth in pelitic schists: implications for thermobarometry and P-T path determinations: Journal of Metamorphic Geology, v. 8, p. 683–696, doi: 10.1111/j.1525-1314.1990.tb00495.x.

Spear, F.S., and Pyle, J.M., 2002, Apatite, monazite, and xenotime in metamorphic rocks, Reviews in Mineralogy and Geochemistry, v. 48, p. 293–335, doi:10.2138/rmg.2002.48.7.

Stacey, J.S. and Kramers, J.D., 1975, Approximation of terrestrial lead evolution by a two-stage model: Earth and Planetary Science Letters, v. 26, p. 207-221.

Szulc, A.G., Najman, Y., Sinclair, H.D., Pringle, M., Bickle, M., Chapman, H., Garzanti, E., Andò, S., Huyghe, P., Mugnier, J.–L., Ojha, T., and DeCelles, P., 2006, Tectonic evolution of the Himalaya constrained by detrital ^{40}Ar–^{39}Ar, Sm–Nd and petrographic data from the Siwalik foreland basin succession, SW Nepal: Basin Research, v. 18, p. 375–391, doi: 10.1111/j.1365-2117.2006.00307.x.

Tamponi, M., Bertoli, M., Innocenti, F., and Leoni, L., 2002-2003, X-Ray fluorescence analysis of major elements in silicate rocks using fused glass discs: Atti Società Toscana di Scienze Naturali, Memorie Serie A, v. 108, p. 73–79.

Vance, D., and Mahar, E., 1998, Pressure-temperature paths from P-T pseudosections and zoned garnets: potential, limitation and examples from Zanskar Himalaya, NW India: Contribution to Mineralogy and Petrology, v. 132, p. 225-245, doi: 10.1007/s004100050419.

Upreti, B.N., 1999, An overview of the stratigraphy and tectonics of the Nepal Himalaya: Journal of Asian Earth Sciences, v. 17, p. 577-606, doi:10.1016/S1367-9120(99)00047-4.

Vannay, J.C., and Hodges, K.V., 1996, Tectonometamorphic evolution of the Himalayan metamorphic core between the Annapurna and Dhaulagiri, central Nepal: Journal of Metamorphic Geology, v. 14, p. 635–656, doi: 10.1046/j.1525-1314.1996.00426.x.

Vannay, J.C., and Grasemann, B., 2001, Himalayan inverted metamorphism and syn-convergence extension as a consequence of a general shear extrusion: Geological Magazine, v.138, p. 253–276, doi:http://dx.doi.org/10.1017/S0016756801005313.

Visonà, D., and Lombardo, B., 2002, Two-mica and tourmaline leucogranites from Everest–Makalu region (Nepal–Tibet). Himalayan leucogranites genesis by isobathic heating?: Lithos, v. 62, p. 125–150, doi:10.1016/S0024-4937(02)00112-3.

Visonà, D., Carosi, R., Montomoli, C., Peruzzo, L., and Tiepolo, M., 2012, Miocene andalusite leucogranite in central-east Himalaya (Everest–Masang Kang area): low-pressure melting during heating: Lithos, v. 144–145, p. 194–208, doi:10.1016/j.lithos.2012.04.012.

Wang, J.M., Zhang, J.J., and Wang, X.X., 2013, Structural kinematics, metamorphic P–T profiles and zircon geochronology across the Greater Himalayan Crystalline Complex in south-central Tibet: implication for a revised channel flow: Journal of Metamorphic Geology, v. 31, p. 607–628, doi:10.1111/jmg.12036.

Wang, J.M., Rubatto, D., and Zhang, J.J., 2015, Timing of Partial Melting and Cooling across the Greater Himalayan Crystalline Complex (Nyalam, Central Himalaya): In-sequence Thrusting and its Implications: Journal of Petrology, v. 56, p. 1677–1702, doi:10.1093/petrology/egv050.

Webb, A.A.G., Yin, A., Harrison, T.M., Célérier, J., and Burgess, P.W., 2007, The leading edge of the Greater Himalayan Crystalline complex revealed in the NW Indian Himalaya: Implications for the evolution of the Himalayan orogen. Geology, v. 35, p. 955-958, doi:10.1130/G23931A.1.

Weller, O.M., St-Onge, M.R., Waters, D.J., Rayner, N., Searle, M.P., Chung, S-L., Palin, R.M., Lee, Y-H., and Xu, X., 2013, Quantifying Barrovian metamorphism in the Danba Structural Culmination of eastern Tibet: Journal of Metamorphic Geology, v. 31, p. 909-935, doi: 10.1111/jmg.12050.

Williams, I.S., 1998, U-Th-Pb geochronology by ion microprobe. In: McKibben, M.A., Shanks, III W.C. and Ridley, W.I. (eds) Application of microanalytical techniques to understanding mineralizing processes, vol 7. Reviews in Economic Geology, Society of Economic Geologists, pp 1-35

Williams, M.L., and Jercinovic, M.J., 2002, Microprobe monazite geochronology: putting absolute time into microstructural analysis: Journal of Structural Geology, v. 24, p. 1013–1028, doi:10.1016/S0191-8141(01)00088-8.

Williams, M.L., and Jercinovic, M.J., 2012, Tectonic interpretation of metamorphic tectonites: integrating compositional mapping, microstructural analysis and in situ monazite dating: Journal of Metamorphic Geology, v. 30, p. 739–752, doi: 10.1111/j.1525-1314.2012.00995.x.

White, R.W., Powell, R., and Holland, T.J.B., 2001, Calculation of partial melting equilibria in the system Na_2O-CaO-K_2O-FeO-MgO-Al_2O_3-SiO_2-H_2O (NCKFMASH): Journal of Metamorphic Geology, v. 19, p. 139-53, doi: 10.1046/j.0263-4929.2000.00303.x.

Whitney, D.L., and Evans, B.W., 2010, Abbreviation for names of rock-forming minerals: American Mineralogist, v. 95, p. 185-187, doi: 10.2138/am.2010.3371.

Yakymchuk, C., and Godin, L., 2012, Coupled role of deformation and metamorphism in the construction of inverted metamorphic sequences: an example from far northwest Nepal: Journal of Metamorphic Geology, v. 30, p. 513–535, doi:10.1111/j.1525-1314.2012.00979.x.

Yin, A., 2006, Cenozoic tectonic evolution of the Himalayan orogen as constrained by along-strike variation of structural geometry, exhumation history, and foreland sedimentation: Earth-Science Reviews, v. 76, p. 1-131, doi:10.1016/j.earscirev.2005.05.004.

Figure captions

Figure 1. (a) Simplified geological map of the Central Himalaya (modified after Ambrose et al., 2015). The study area is indicated by the dotted box. (b) Geological sketch map of the Kali Gandaki valley with location of the Kalopani Shear Zone, the samples in this study (KL-19, KL-21) and samples of the K28 series of Carosi et al. (2015) and Iaccarino et al. (2015). Stereographic projection of the main foliation planes (S_2) and object lineation (Lext) are shown in the insert in the upper right. 1 Quartzite (LHS); 2: Kyanite gneiss (GHS); 3: Calcsilicate and marble (GHS); 4: Metapelite (GHS); 5: Orthogneiss (GHS); 6: Tethyan Sedimentary Sequences (TSS); 7: Alluvial debris; 8: South Tibetan Detachment; 9: Minor normal fault; 10: Kalopani shear zone; 11: High Himalayan Discontinuity according to Iaccarino et al. (2015) and Main Central Thrust close to Dana village (according to Colchen et al. 1986; Vannay and Hodges 1996 and Carosi et al. 2014); 12: Main foliation; 13: object lineation; 14: location of samples quoted in the text.

Figure 2. Detailed geological map of the Kalopani Shear Zone.

Figure 3. Orthogneiss of Unit 3 of the GHS sheared by the Kalopani Shear Zone and position of the sample KL-21. Asymmetric fabric points to a top-to-the S–SW sense of shear.

Figure 4. Microscopic features of Kalopani Shear Zone samples: (a) paragneiss KL-19, with top-to-the-S shearing; (b) Garnet and staurolite crystals in KL-19. Note the internal foliation in garnet (S_i); (c) general view of KL-21 sample, showing Grain Boundary Migration in quartz; (d) pinning microstructures in quartz of KL-21.

Figure 5 Representative X-ray maps for Mg, Ca, Mn and Fe in garnet. The line C-R refers to the core-rim profile in (b), the scale bar is 750 µm. In the Mg map the ellipse indicates the monazite (Mnz 334) included in garnet; (b) Core to rim normalized profiles through garnet.

Figure 6. P-T pseudosection for paragneiss KL-19. The observed equilibrium assemblage is highlighted. Minerals abbreviation after Whitney and Evans (2010) except for fluid phase, white mica and silicate melt indicated by V, Wm and L, respectively.

Figure 7. Details of isopleth contouring for: (a) XCa (i.e. Ca/(Ca+Mg+Mn+Fe)) in garnet (Grt); (b) XMg (i.e. Mg/(Ca+Mg+Mn+Fe)) in garnet; (c) Si^{4+} (p.f.u.) in white mica; (d) XMg in staurolite; (e) Na/Na+Ca (i.e. XAb) in the plagioclase feldspar and (f) modal amount of garnet (Vol% Grt) in 100% solids.

Figure 8. Sketch of the P-T path for the sheared paragneiss (sample KL-19), based on pseudosection calculation, THERMOCALC average PT (AvePT), and Ti-in biotite thermometry. Abbreviations as in Fig. 6.

Figure 9. (a) Chemistry of monazite in the system $2REEPO_4$–$CaTh(PO_4)_2$–$2ThSiO_4$, after Linthout (2007); (b) Plot of cheralite and huttonite exchange vectors; (c) Heavy Rare Earth Elements (HREE and Y) versus Light Rare Earth Elements (LREE) plot of monazite.

Figure 10. U-Th-Pb concordia diagrams for KL-21 and KL-19 monazite analysed by LA-ICP-MS. Only data with <10% of discordance are shown. Quoted errors are at 2σ level.

Figure 11 Conventional Concordia plot (left) for U-Pb SHRIMP analyses of monazite and representative BSE image (right) of dated monazite crystal from paragneiss KL-19. White numbers in the BSE image indicate $^{206}Pb/^{238}U$ ages and absolute errors (±1 sigma) whereas green numbers indicate LA-ICP-MS ages.

Figure 12. Cumulative histogram and probability curve of LA–ICP–MS and SHRIMP $^{206}Pb/^{238}U$ ages differentiated by methods, sample and textural position.

Figure 13. Sketch of the evolution of the GHS by progressive activation of top-to-the-SW shear zones from the uppermost part to the lower part. The kinematic path of particles in the hanging wall and footwall of the detected ductile shear zones in the GHS is shown by squares with different colors. At ~ 41-30 Ma the hanging wall of the KSZ was exhuming whereas the footwall was still undergoing prograde metamorphism. At 26-24 Ma, following the activation of the HHD, the GHS1 and 2 in the hanging wall of the HHS started exhumation whereas rocks in the footwall of the HHD were still buried. At 17-12 Ma the activation of the MCT caused the exhumation of all sub-units of the GHS (GHS 1, 2 3) and the LHS was incorporated in the belt. GHS1, 2, 3: tectonic sub-units of the Greater Himalayan Sequence (GHS); TSS: Tethyan Sedimentary Sequence; Grey areas: leucogranites emplaced in the time span 19-24 Ma (Bertoldi et al., 211; Carosi et al., 2013); KSZ: Kalopani Shear Zone; HHD: High Himalayan Discontinuity (Montomoli et al., 2013, 2015; Iaccarino et al., 2015); MCT: Main Central Thrust; LHS: Lesser Himalayan Sequence. Not to scale.

List of tables

Table 1. Representative EMP analyses (in wt%) of minerals in the paragneiss sample KL-19 (formulae were calculated on the following basis: garnet = 24 O, 8 cations; staurolite = 46 O; micas = 11 O; chlorite = 28 O; feldspar = 8 O; spinel = 4 O, 3 cations; ilmenite = 3 O).

Table 2. Representative EMP analyses of monazite (recalculated on the basis of 4 O) from the dated samples (KL-19 and KL-21).

Table 3. Summary of monazite LA-ICP-MS isotopic results for sample KL-19 and KL-21.

Table 4. SHRIMP U-Th-Pb analyses of monazite in samples KL-21 and KL-19.

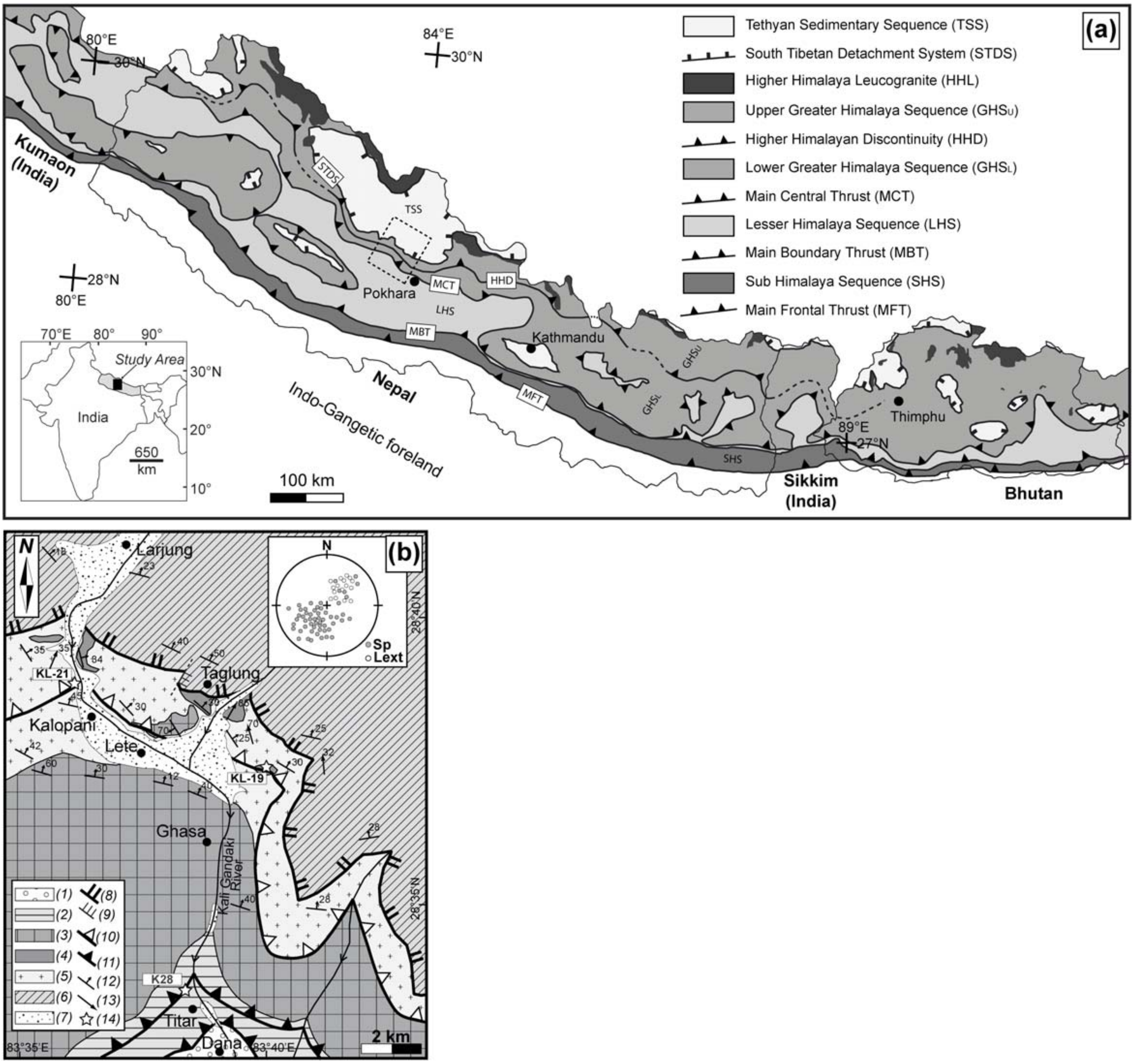
(a)
Tethyan Sedimentary Sequence (TSS)
South Tibetan Detachment System (STDS)
Higher Himalaya Leucogranite (HHL)
Upper Greater Himalaya Sequence (GHSU)
Higher Himalayan Discontinuity (HHD)
Lower Greater Himalaya Sequence (GHSL)
Main Central Thrust (MCT)
Lesser Himalaya Sequence (LHS)
Main Boundary Thrust (MBT)
Sub Himalaya Sequence (SHS)
Main Frontal Thrust (MFT)
80°E
30°N
84°E
30°N
Kumaon (India)
STDS
TSS
28°N
80°E
Pokhara
MCT
HHD
LHS
MBT
Kathmandu
Study Area
30°N
India
20°
10°
650 km
Nepal
Indo-Gangetic foreland
MFT
GHSU
GHSL
Thimphu
89°E
27°N
SHS
100 km
Sikkim (India)
Bhutan
(b)
N
Larjung
Sp
Lext
KL-21
Taglung
Kalopani
Lete
KL-19
Ghasa
Kali Gandaki River
K28
Titar
Dana
28°40'N
28°35'N
83°35'E
83°40'E
2 km
(1)
(2)
(3)
(4)
(5)
(6)
(7)
(8)
(9)
(10)
(11)
(12)
(13)
(14)

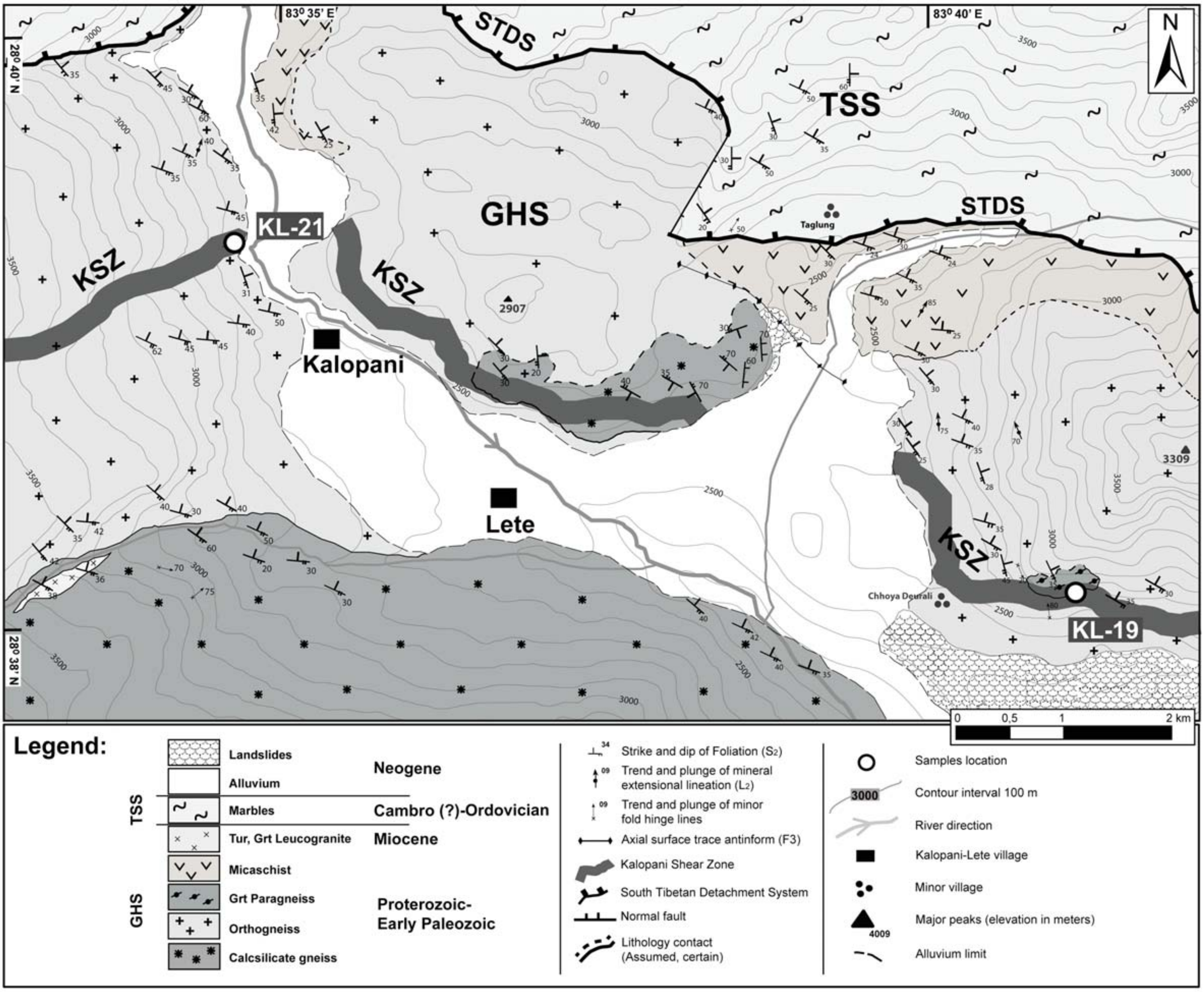

83° 35' E
83° 40' E
28° 40' N
28° 38' N
N
STDS
TSS
GHS
KSZ
KL-21
KL-19
Kalopani
Lete
Taglung
Chhoya Deurali
2907
3309
0 0,5 1 2 km
Legend:
Landslides
Alluvium
Neogene
TSS
Marbles
Cambro (?)-Ordovician
Tur, Grt Leucogranite
Miocene
Micaschist
GHS
Grt Paragneiss
Orthogneiss
Calcsilicate gneiss
Proterozoic-Early Paleozoic
Strike and dip of Foliation (S2)
Trend and plunge of mineral extensional lineation (L2)
Trend and plunge of minor fold hinge lines
Axial surface trace antiform (F3)
Kalopani Shear Zone
South Tibetan Detachment System
Normal fault
Lithology contact (Assumed, certain)
Samples location
Contour interval 100 m
River direction
Kalopani-Lete village
Minor village
Major peaks (elevation in meters)
Alluvium limit

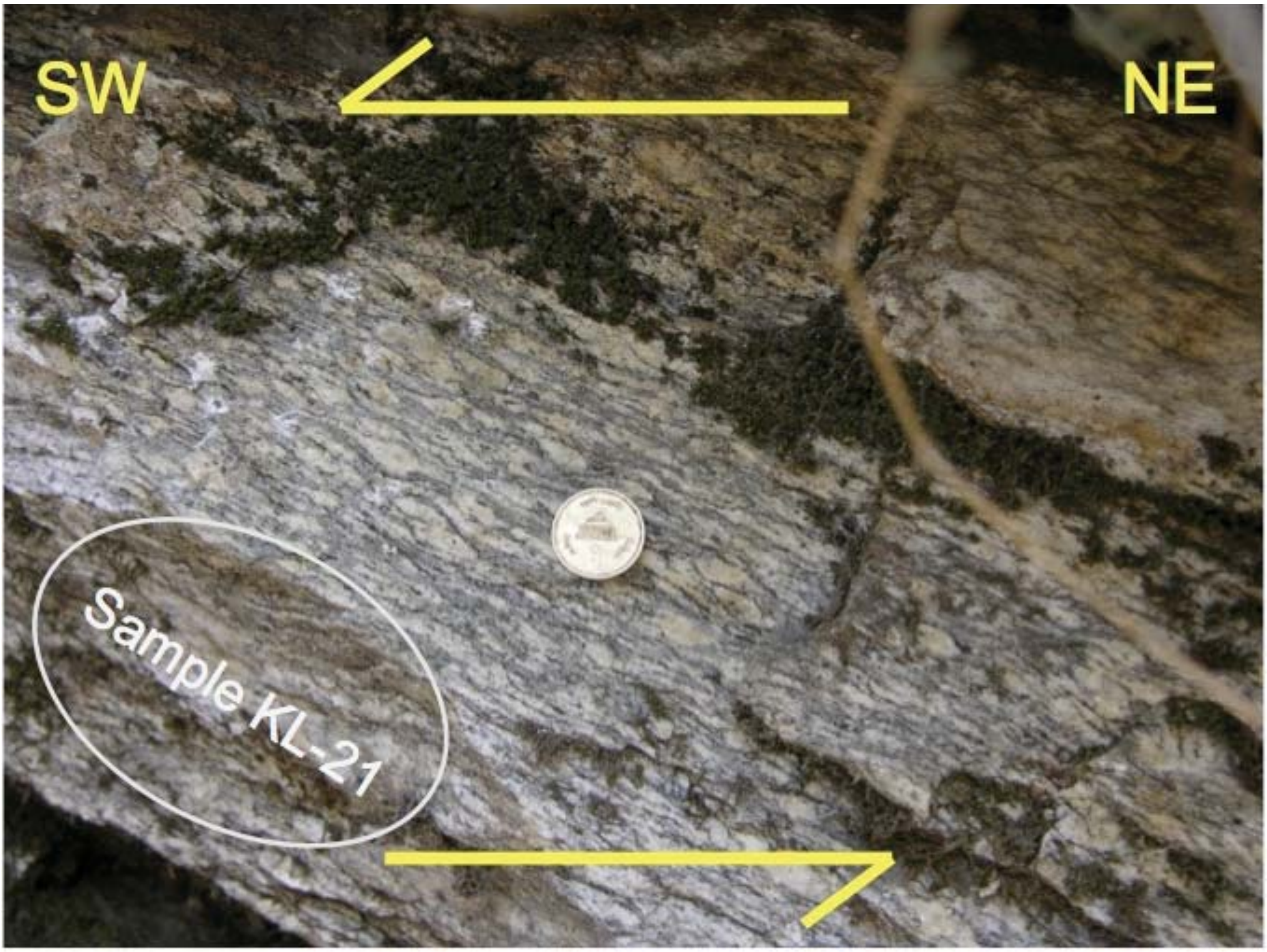

SW
NE
Sample KL-21

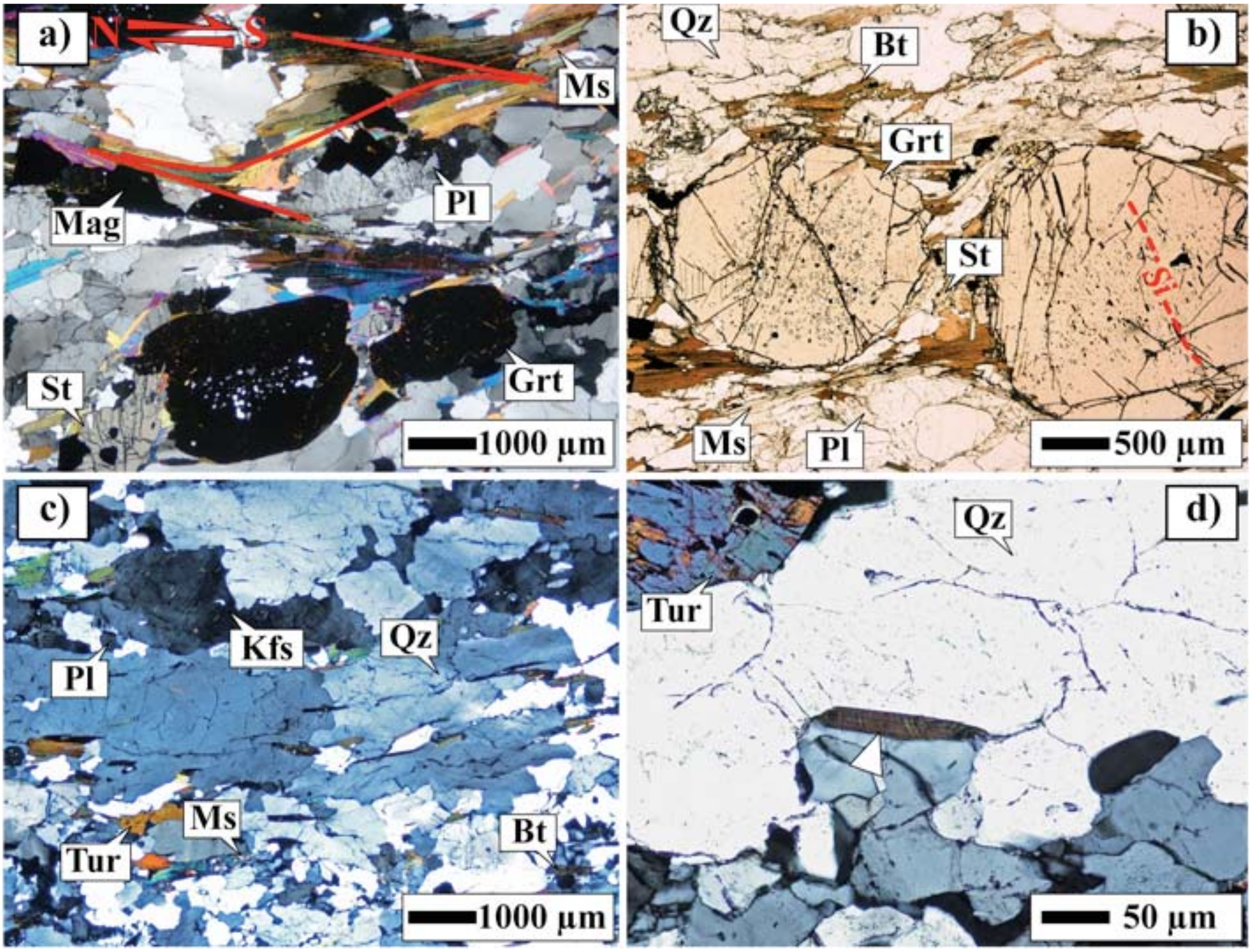
a)
N
S
Ms
Pl
Mag
Grt
St
1000 µm
b)
Qz
Bt
Grt
St
Si
Ms
Pl
500 µm
c)
Kfs
Qz
Pl
Ms
Tur
Bt
1000 µm
d)
Qz
Tur
50 µm

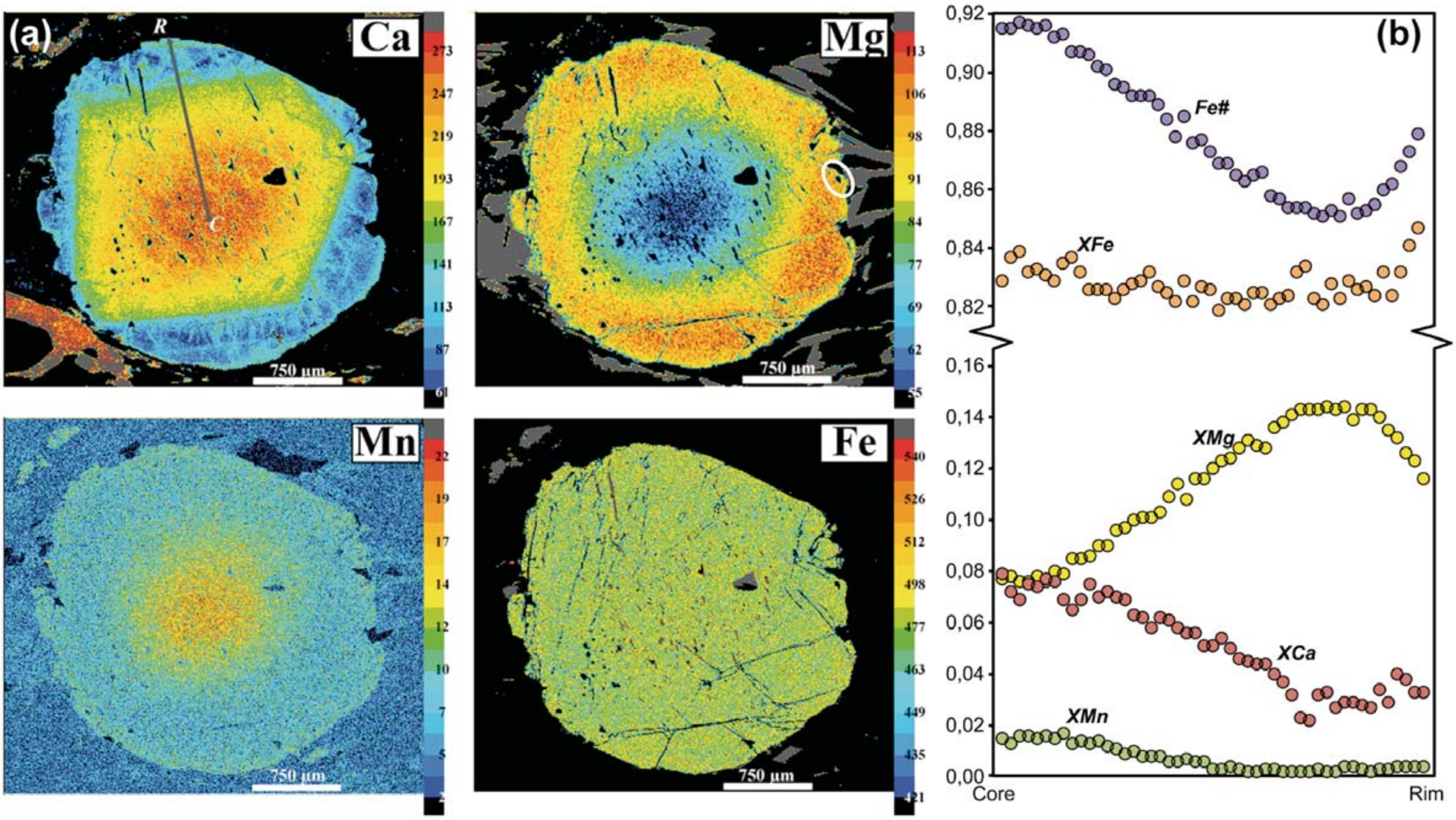
(a)
R
C
Ca
273
247
219
193
167
141
113
87
61
750 µm
Mg
113
106
98
91
84
77
69
62
55
750 µm
Mn
22
19
17
14
12
10
7
5
750 µm
Fe
540
526
512
498
477
463
449
435
421
750 µm
(b)
0,92
0,90
0,88
0,86
0,84
0,82
0,16
0,14
0,12
0,10
0,08
0,06
0,04
0,02
0,00
Fe#
XFe
XMg
XCa
XMn
Core
Rim

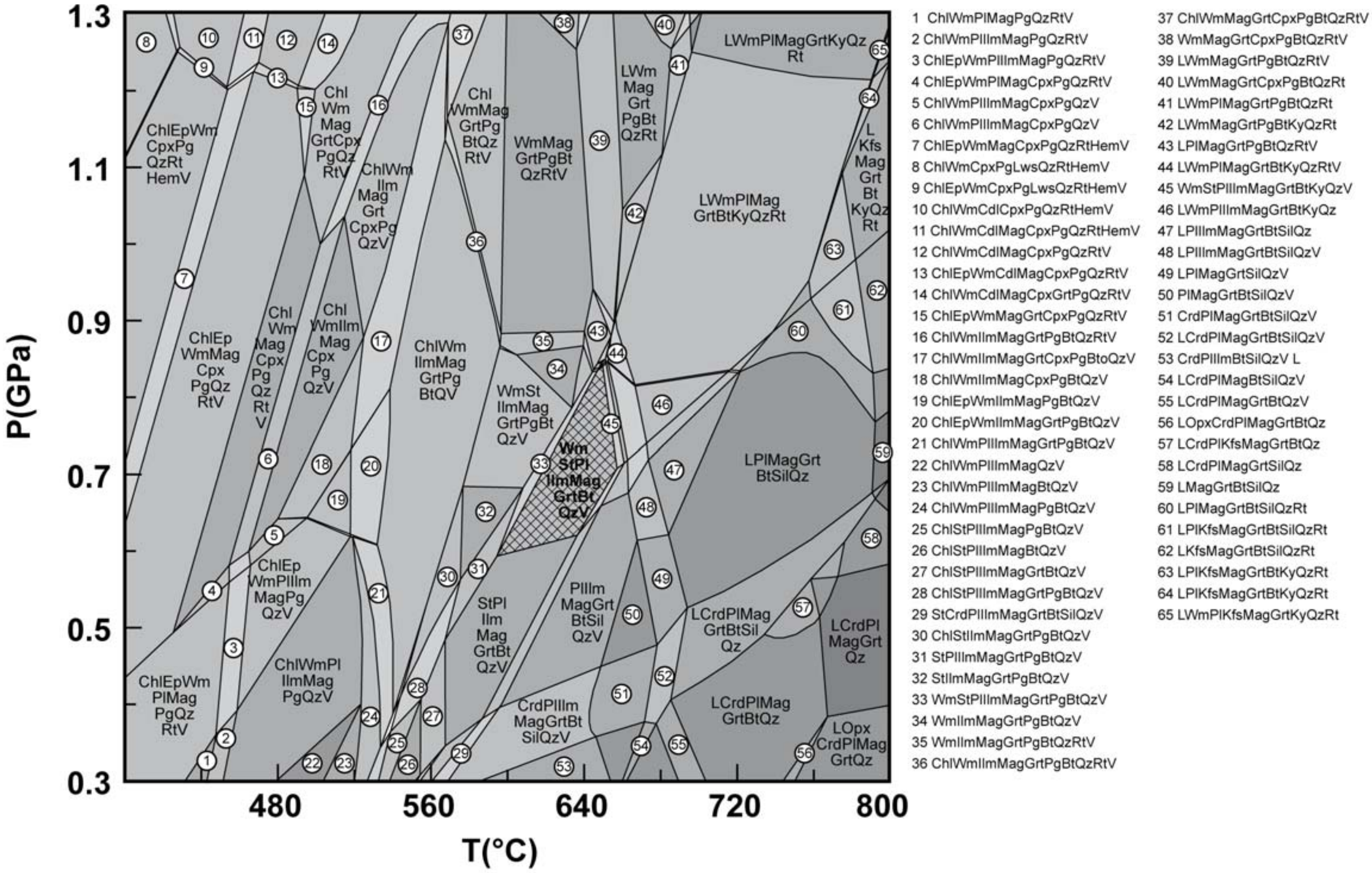

P(GPa)
1.3
1.1
0.9
0.7
0.5
0.3
T(°C)
480
560
640
720
800
ChlEpWm CpxPg QzRt HemV
ChlEp WmMag Cpx PgQz RtV
ChlEpWm PlMag PgQz RtV
ChlEp WmPlIlm MagPg QzV
ChlWmPl IlmMag PgQzV
Chl Wm Mag Cpx Pg Qz Rt V
Chl WmIlm Mag Cpx Pg QzV
Chl Wm Mag GrtCpx PgQz RtV
ChlWm Ilm Mag Grt CpxPg QzV
ChlWm IlmMag GrtPg BtQV
Chl WmMag GrtPg BtQz RtV
WmMag GrtPgBt QzRtV
LWm Mag Grt PgBt QzRt
LWmPlMagGrtKyQz Rt
LWmPlMag GrtBtKyQzRt
L Kfs Mag Grt Bt KyQz Rt
WmSt IlmMag GrtPgBt QzV
Wm StPl IlmMag GrtBt QzV
StPl Ilm Mag GrtBt QzV
PlIlm MagGrt BtSil QzV
CrdPlIlm MagGrtBt SilQzV
LPlMagGrt BtSilQz
LCrdPlMag GrtBtSil Qz
LCrdPlMag GrtBtQz
LCrdPl MagGrt Qz
LOpx CrdPlMag GrtQz
1 ChlWmPlMagPgQzRtV
2 ChlWmPlIlmMagPgQzRtV
3 ChlEpWmPlIlmMagPgQzRtV
4 ChlEpWmPlMagCpxPgQzRtV
5 ChlWmPlIlmMagCpxPgQzV
6 ChlWmPlIlmMagCpxPgQzV
7 ChlEpWmMagCpxPgQzRtHemV
8 ChlWmCpxPgLwsQzRtHemV
9 ChlEpWmCpxPgLwsQzRtHemV
10 ChlWmCdlCpxPgQzRtHemV
11 ChlWmCdlMagCpxPgQzRtHemV
12 ChlWmCdlMagCpxPgQzRtV
13 ChlEpWmCdlMagCpxPgQzRtV
14 ChlWmCdlMagCpxGrtPgQzRtV
15 ChlEpWmMagGrtCpxPgQzRtV
16 ChlWmIlmMagGrtPgBtQzRtV
17 ChlWmIlmMagGrtCpxPgBtoQzV
18 ChlWmIlmMagCpxPgBtQzV
19 ChlEpWmIlmMagPgBtQzV
20 ChlEpWmIlmMagGrtPgBtQzV
21 ChlWmPlIlmMagGrtPgBtQzV
22 ChlWmPlIlmMagQzV
23 ChlWmPlIlmMagBtQzV
24 ChlWmPlIlmMagPgBtQzV
25 ChlStPlIlmMagPgBtQzV
26 ChlStPlIlmMagBtQzV
27 ChlStPlIlmMagGrtBtQzV
28 ChlStPlIlmMagGrtPgBtQzV
29 StCrdPlIlmMagGrtBtSilQzV
30 ChlStIlmMagGrtPgBtQzV
31 StPlIlmMagGrtPgBtQzV
32 StIlmMagGrtPgBtQzV
33 WmStPlIlmMagGrtPgBtQzV
34 WmIlmMagGrtPgBtQzV
35 WmIlmMagGrtPgBtQzRtV
36 ChlWmIlmMagGrtPgBtQzRtV
37 ChlWmMagGrtCpxPgBtQzRtV
38 WmMagGrtCpxPgBtQzRtV
39 LWmMagGrtPgBtQzRtV
40 LWmMagGrtCpxPgBtQzRt
41 LWmPlMagGrtPgBtQzRt
42 LWmMagGrtPgBtKyQzRt
43 LPlMagGrtPgBtQzRtV
44 LWmPlMagGrtBtKyQzRtV
45 WmStPlIlmMagGrtBtKyQzV
46 LWmPlIlmMagGrtBtKyQz
47 LPlIlmMagGrtBtSilQz
48 LPlIlmMagGrtBtSilQzV
49 LPlMagGrtSilQzV
50 PlMagGrtBtSilQzV
51 CrdPlMagGrtBtSilQzV
52 LCrdPlMagGrtBtSilQzV
53 CrdPlIlmBtSilQzV L
54 LCrdPlMagBtSilQzV
55 LCrdPlMagGrtBtQzV
56 LOpxCrdPlMagGrtBtQz
57 LCrdPlKfsMagGrtBtQz
58 LCrdPlMagGrtSilQz
59 LMagGrtBtSilQz
60 LPlMagGrtBtSilQzRt
61 LPlKfsMagGrtBtSilQzRt
62 LKfsMagGrtBtSilQzRt
63 LPlKfsMagGrtBtKyQzRt
64 LPlKfsMagGrtBtKyQzRt
65 LWmPlKfsMagGrtKyQzRt

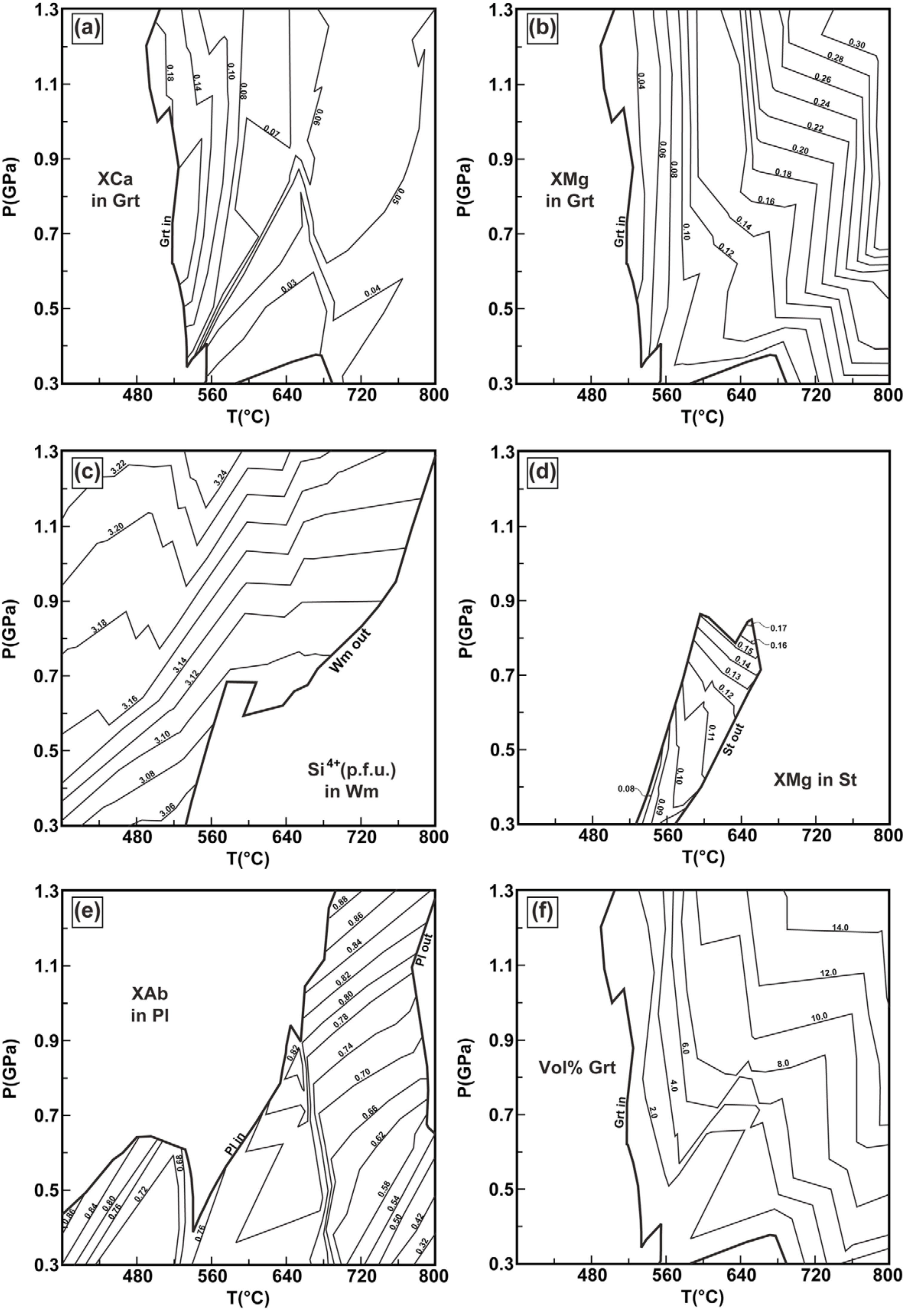

(a)
XCa
in Grt
Grt in
0.18
0.14
0.10
0.08
0.07
0.06
0.05
0.03
0.04
(b)
XMg
in Grt
Grt in
0.04
0.06
0.08
0.10
0.12
0.14
0.16
0.18
0.20
0.22
0.24
0.26
0.28
0.30
(c)
Si4+(p.f.u.)
in Wm
Wm out
3.22
3.24
3.20
3.18
3.16
3.14
3.12
3.10
3.08
3.06
(d)
XMg in St
St out
0.17
0.16
0.15
0.14
0.13
0.12
0.11
0.10
0.09
0.08
(e)
XAb
in Pl
Pl in
Pl out
0.88
0.86
0.84
0.82
0.80
0.78
0.74
0.70
0.66
0.62
0.58
0.54
0.50
0.42
0.32
0.82
0.86
0.84
0.80
0.76
0.72
0.68
0.76
(f)
Vol% Grt
Grt in
14.0
12.0
10.0
8.0
6.0
4.0
2.0
P(GPa)
T(°C)
1.3
1.1
0.9
0.7
0.5
0.3
480
560
640
720
800

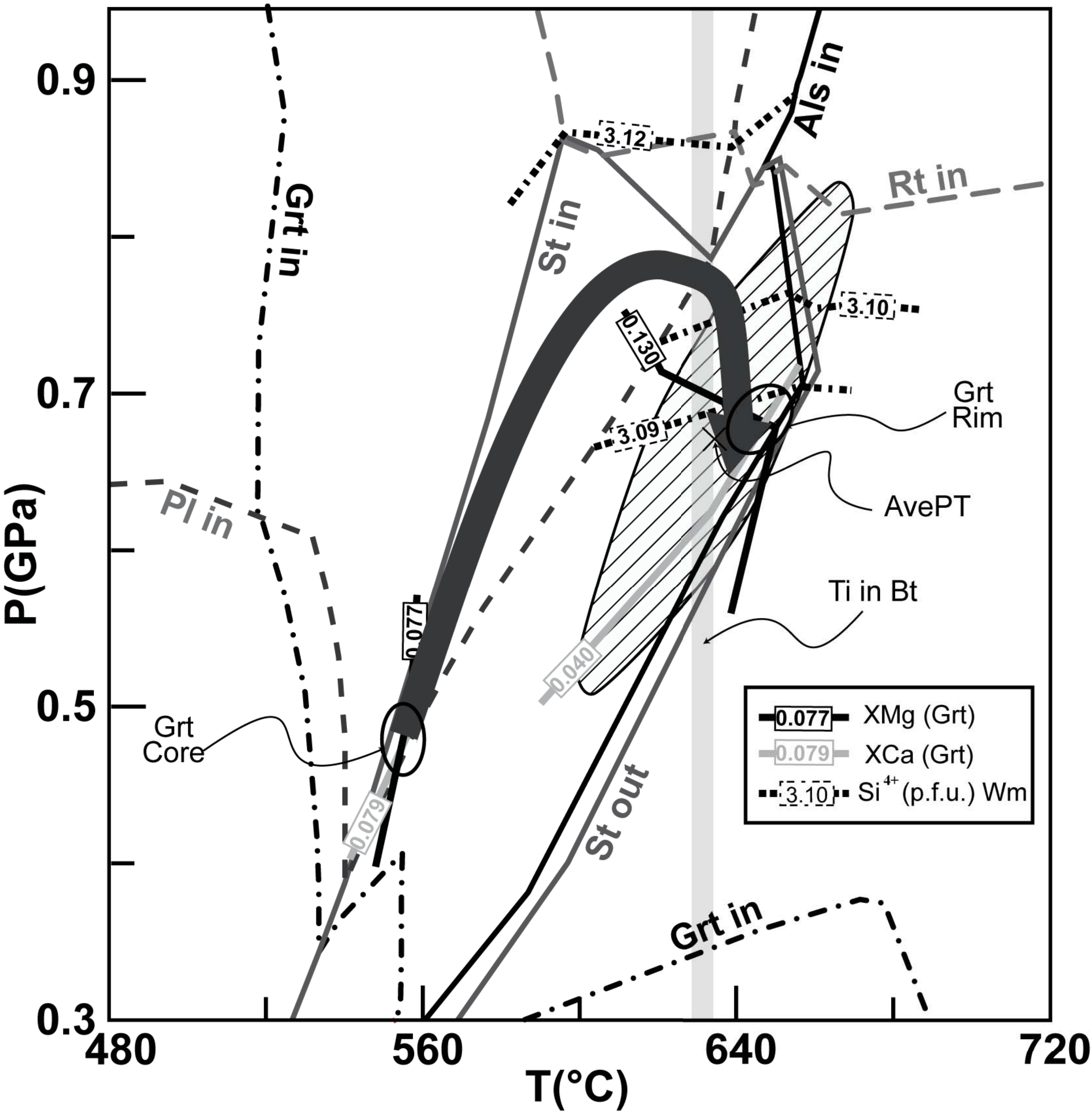

P(GPa)
T(°C)
0.9
0.7
0.5
0.3
480
560
640
720
Grt in
St in
Als in
Rt in
Pl in
St out
Grt in
3.12
3.10
3.09
0.130
0.077
0.079
0.040
Grt
Rim
AvePT
Ti in Bt
Grt
Core
0.077 XMg (Grt)
0.079 XCa (Grt)
3.10 Si^{4+} (p.f.u.) Wm

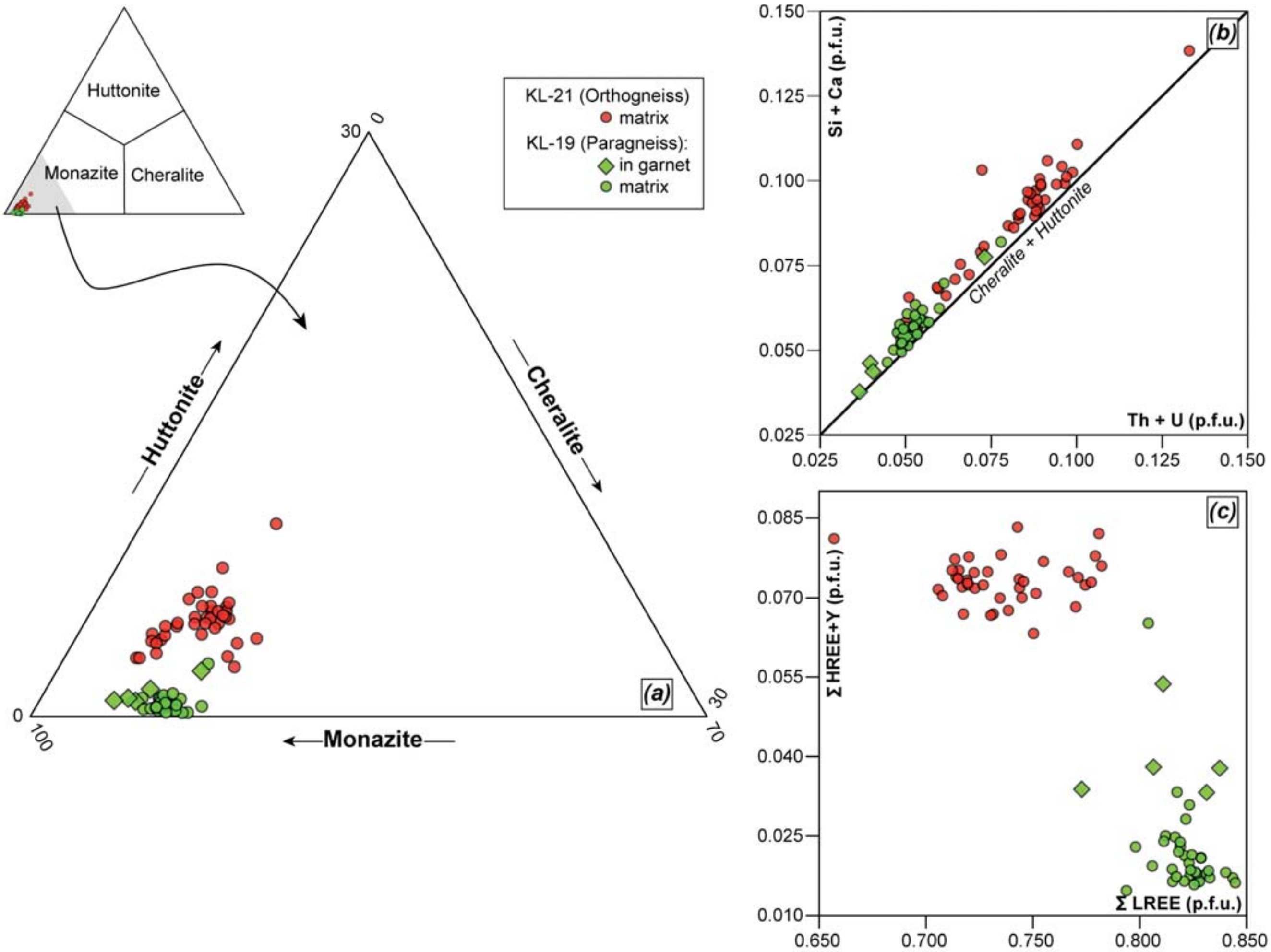

Huttonite
Monazite
Cheralite
KL-21 (Orthogneiss)
matrix
KL-19 (Paragneiss):
in garnet
matrix
30
0
Huttonite
Cheralite
Monazite
(a)
0
100
30
70
Si + Ca (p.f.u.)
Th + U (p.f.u.)
Cheralite + Huttonite
(b)
0.150
0.125
0.100
0.075
0.050
0.025
0.025
0.050
0.075
0.100
0.125
0.150
Σ HREE+Y (p.f.u.)
Σ LREE (p.f.u.)
(c)
0.085
0.070
0.055
0.040
0.025
0.010
0.650
0.700
0.750
0.800
0.850

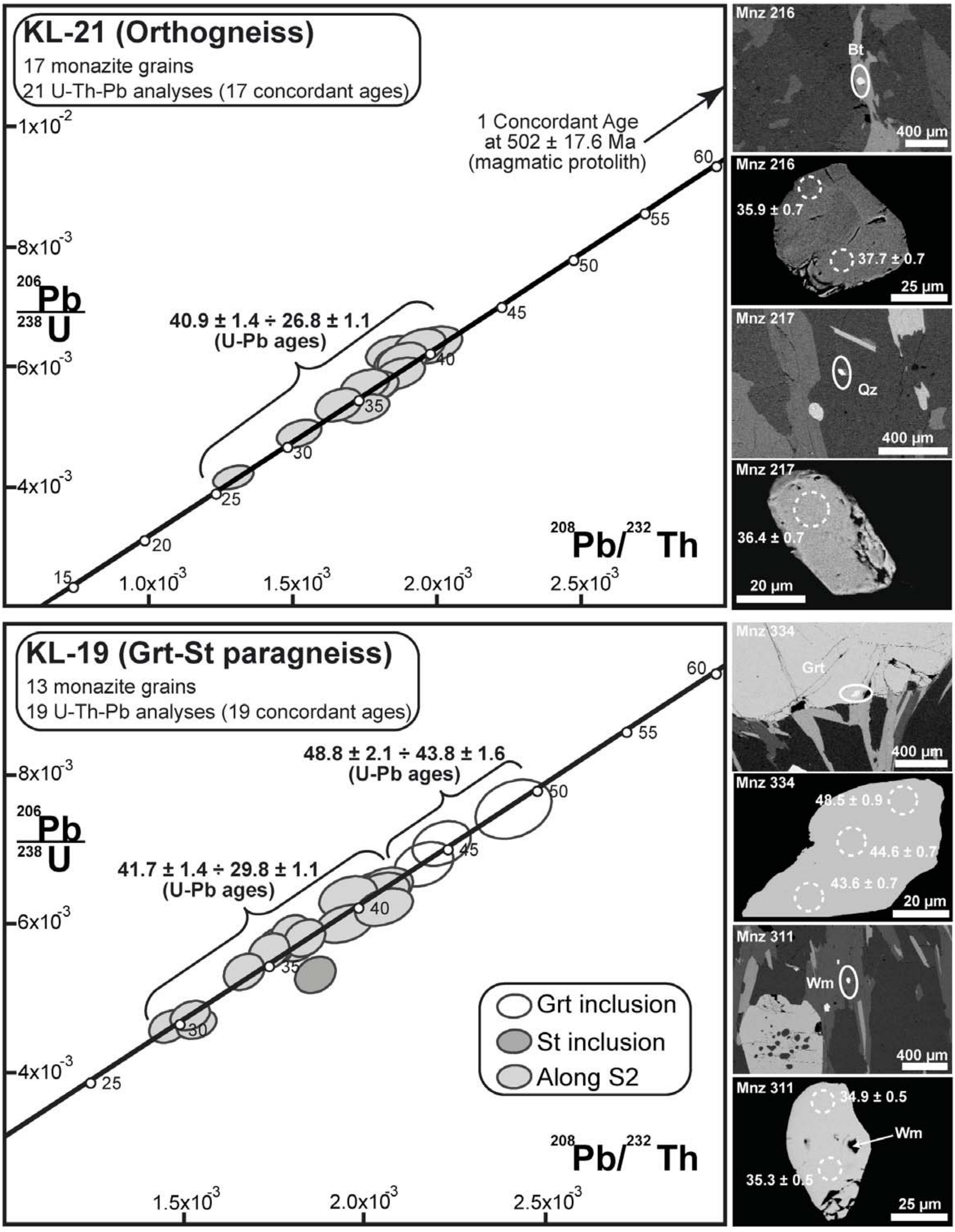
KL-21 (Orthogneiss)
17 monazite grains
21 U-Th-Pb analyses (17 concordant ages)
1 Concordant Age at 502 ± 17.6 Ma (magmatic protolith)
40.9 ± 1.4 ÷ 26.8 ± 1.1 (U-Pb ages)
206Pb/238U
208Pb/232Th
1x10-2
8x10-3
6x10-3
4x10-3
1.0x10-3
1.5x10-3
2.0x10-3
2.5x10-3
15
20
25
30
35
40
45
50
55
60
Mnz 216
Bt
400 µm
35.9 ± 0.7
37.7 ± 0.7
25 µm
Mnz 217
Qz
36.4 ± 0.7
20 µm
KL-19 (Grt-St paragneiss)
13 monazite grains
19 U-Th-Pb analyses (19 concordant ages)
48.8 ± 2.1 ÷ 43.8 ± 1.6 (U-Pb ages)
41.7 ± 1.4 ÷ 29.8 ± 1.1 (U-Pb ages)
Grt inclusion
St inclusion
Along S2
Mnz 334
Grt
48.5 ± 0.9
44.6 ± 0.7
43.6 ± 0.7
Mnz 311
Wm
34.9 ± 0.5
35.3 ± 0.5

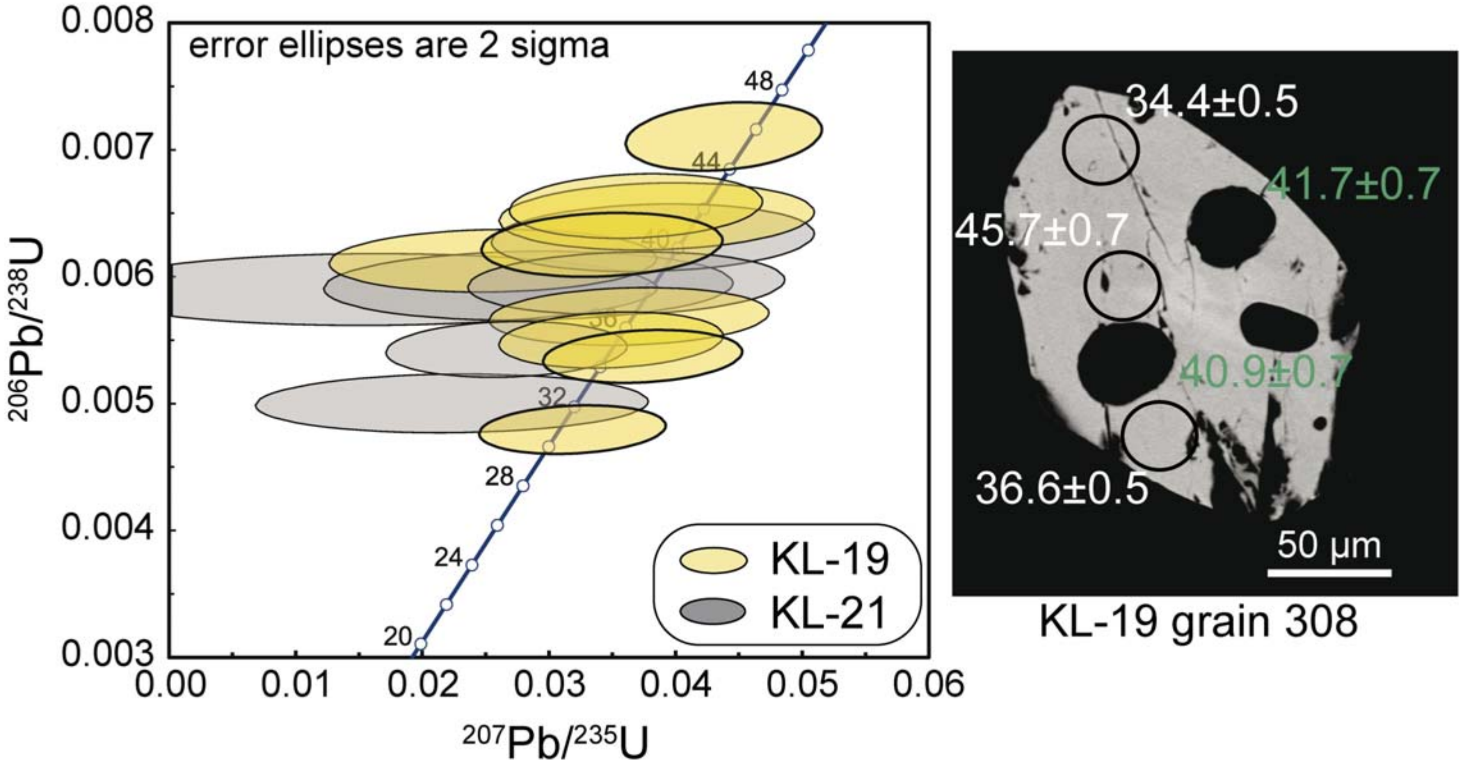

KL-19 grain 308

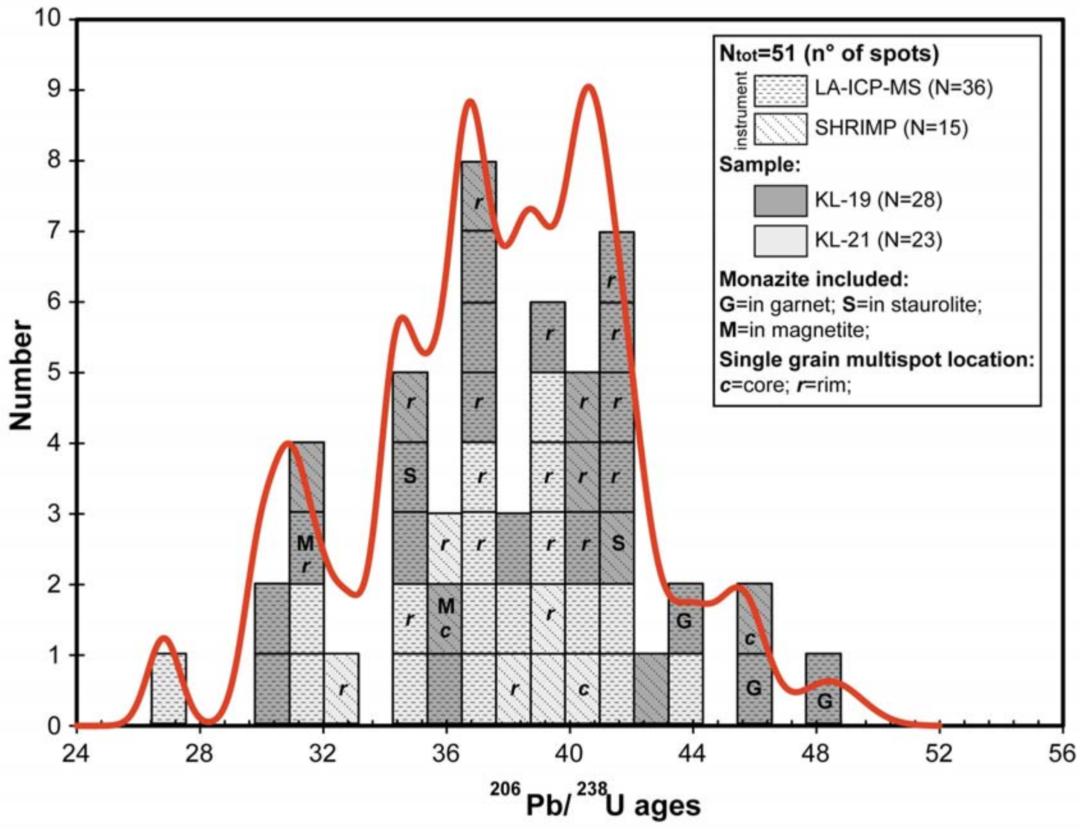

Ntot=51 (n° of spots)
instrument
LA-ICP-MS (N=36)
SHRIMP (N=15)
Sample:
KL-19 (N=28)
KL-21 (N=23)
Monazite included:
G=in garnet; S=in staurolite;
M=in magnetite;
Single grain multispot location:
c=core; r=rim;
Number
206Pb/238U ages

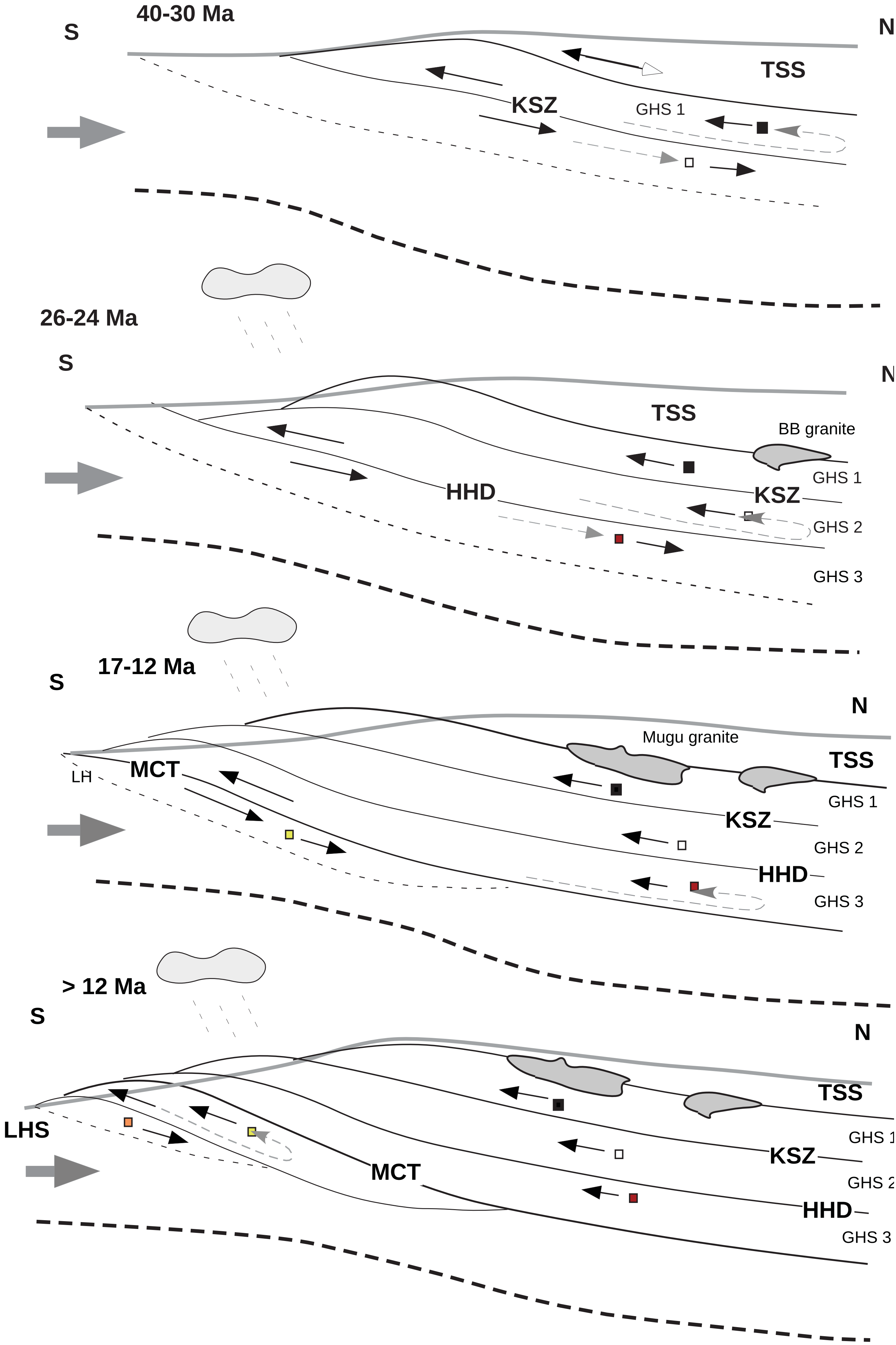
40-30 Ma
S
N
TSS
KSZ
GHS 1
26-24 Ma
S
N
TSS
BB granite
GHS 1
KSZ
HHD
GHS 2
GHS 3
17-12 Ma
S
N
Mugu granite
TSS
MCT
LH
GHS 1
KSZ
GHS 2
HHD
GHS 3
> 12 Ma
S
N
TSS
LHS
GHS 1
KSZ
GHS 2
MCT
HHD
GHS 3

Table 1

Minerals:	Grt core	Grt middle	Grt rim	St core	St rim	Bt in Grt	Bt matrix	Ms matrix	Ms matrix	Pl matrix	Pl matrix	Opaque matrix	Ilm matrix
SiO_2	35.41	35.98	35.32	27.40	27.58	36.50	35.62	45.41	46.20	63.67	64.26	0.00	0.00
TiO_2	0.02	0.01	0.00	0.63	0.66	1.16	2.44	0.60	0.51			0.09	48.57
Al_2O_3	20.85	21.05	20.98	53.77	55.34	18.68	17.47	33.22	32.74	22.08	22.03	0.32	0.00
Cr_2O_3	0.03	0.01	0.00	0.05	0.05							0.12	0.02
FeO_{tot}	38.03	38.41	38.79	14.75	13.33	18.07	22.84	2.91	3.18	0.02	0.03	94.12	50.93
MnO	0.67	0.15	0.17	0.00	0.01	0.03	0.00	0.00	0.01			0.02	0.01
MgO	1.93	3.12	3.33	1.40	0.98	12.19	8.39	0.73	0.87	0.00	0.00	0.00	0.19
ZnO				0.58	0.59							0.04	0.02
CaO	2.72	1.91	1.40	0.01	0.01	0.00	0.10	0.00	0.02	3.81	0.00	0.03	0.00
Na_2O	0.00	0.00	0.01	0.00	0.00	0.39	0.37	1.52	1.40	9.99	3.53		
K_2O				0.00	0.01	8.78	8.77	9.3	9.41	0.06	10.21		
BaO						0.06	0.05	0.11	0.11	0.00	0.05		
Tot.	99.66	100.64	100.00	98.59	98.56	95.86	96.05	93.80	94.45	99.63	100.11	94.74	99.78
Si	5.804	5.806	5.746	7.333	7.347	2.730	2.732	3.094	3.129	2.826	2.837	0.000	0.00
^{IV}Al	0.196	0.194	0.254	0.667	0.653	1.270	1.268	0.906	0.871	1.155	1.146		0.00
Ti	0.002	0.001	0.000	0.127	0.132	0.065	0.141	0.031	0.026			0.003	0.95
^{VI}Al	3.832	3.810	3.770	16.290	16.723	0.376	0.311	1.762	1.742			0.014	0.00
Cr	0.004	0.001	0.000	0.010	0.010							0.004	0.00
Fe^{3+}	0.166	0.189	0.230			0.000	0.000	0.000	0.000	0.001	0.001	1.981	
Fe^{2+}	5.048	4.994	5.049	3.302	2.969	1.130	1.465	0.166	0.180			0.994	1.10
Mn	0.093	0.021	0.023	0.001	0.001	0.002	0.000	0.000	0.001			0.001	0.00
Mg	0.471	0.750	0.244	0.560	0.390	1.359	0.959	0.075	0.088	0.000	0.000	0.000	0.00
Zn				0.114	0.115							0.001	0.00
Ca	0.478	0.330	0.808	0.002	0.002	0.000	0.004	0.000	0.002	0.181	0.167	0.001	0.00
Na	0.000	0.000	0.003	0.001	0.000	0.056	0.055	0.201	0.184	0.860	0.874		
K				0.000	0.003	0.838	0.858	0.809	0.813	0.004	0.003		
Ba						0.002	0.003	0.003	0.003	0.000	0.000		

Table 2

Sample:	KL-21	KL-21	KL-21	KL-21	KL-21	KL-21	Kl-19	Kl-19	Kl-19	Kl-19	Kl-19	Kl-19
Grain:	Mnz217	Mnz216	Mnz216	Mnz240	Mnz240	Mnz226	Mnz 334	Mnz 334	Mnz326	Mnz330	Mnz317	Mnz317
*T. P.:	mic.	Sp	Sp	Sp	Sp	mic.	in Grt	in Grt	in Grt	Sp	Sp	Sp
**S.P..:	core	core	rim	core	rim	core	rim	rim	rim	rim	core	rim
wt%												
P_2O_5	31.46	30.24	31.37	30.07	29.31	31.19	32.08	31.29	31.21	32.29	32.46	33.02
SiO_2	1.17	0.74	0.96	0.63	1.40	1.15	0.23	0.34	0.19	0.07	0.25	0.19
ThO_2	8.97	9.80	6.89	9.67	9.82	9.67	4.42	5.56	4.30	5.50	5.25	5.01
UO_2	0.49	0.58	0.42	0.76	0.65	0.48	0.40	0.37	0.42	0.82	0.51	0.85
La_2O_3	11.75	11.44	12.64	11.84	11.53	11.42	14.36	13.73	13.46	14.41	13.79	14.16
Ce_2O_3	27.40	26.19	28.11	26.58	26.87	26.15	30.49	29.24	29.41	29.49	28.71	29.48
Pr_2O_3	3.07	2.71	3.07	3.00	3.05	2.96	3.12	3.18	3.25	3.24	3.29	3.34
Nd_2O_3	10.37	10.42	10.98	10.29	10.54	10.12	11.25	11.24	11.33	11.35	11.03	11.11
Sm_2O_3	2.23	2.24	2.21	2.13	2.33	2.16	1.91	1.97	2.16	2.06	2.11	2.10
Eu_2O_3	0.31	0.20	0.14	0.30	0.18	0.34	0.49	0.43	0.53	0.53	0.66	0.65
Gd_2O_3	1.67	1.42	1.73	1.69	1.64	1.64	1.16	1.32	1.52	1.20	1.42	1.28
Tb_2O_3	0.00	0.00	0.00	0.00	0.00	0.00	0.00	0.00	0.00	0.00	0.00	0.00
Dy_2O_5	0.66	0.65	0.60	0.60	0.83	0.67	0.25	0.07	0.29	0.09	0.64	0.01
Er_2O_3	0.11	0.01	0.05	0.02	0.19	0.02	0.00	0.00	0.00	0.00	0.00	0.00
Yb_2O_3	0.00	0.00	0.11	0.02	0.01	0.00	0.01	0.00	0.00	0.04	0.00	0.00
Y_2O_3	2.15	2.12	2.22	1.95	2.33	2.23	0.80	1.07	1.60	0.27	2.05	0.29
CaO	1.10	1.57	0.77	1.72	1.08	1.31	0.89	1.05	0.99	1.32	1.02	1.22
Tot.	102.91	100.34	102.28	101.27	101.76	101.50	101.85	100.85	100.65	102.69	103.19	102.70
element												
P	0.992	0.988	0.996	0.982	0.957	0.994	1.020	1.010	1.010	1.022	1.017	1.032
Si	0.044	0.029	0.036	0.024	0.054	0.043	0.008	0.013	0.007	0.002	0.009	0.007
Th	0.076	0.086	0.059	0.085	0.086	0.083	0.038	0.048	0.037	0.047	0.044	0.042
U	0.004	0.005	0.003	0.007	0.006	0.004	0.003	0.003	0.004	0.007	0.004	0.007
La	0.161	0.163	0.175	0.168	0.164	0.159	0.199	0.193	0.190	0.199	0.188	0.193
Ce	0.374	0.370	0.386	0.375	0.380	0.360	0.419	0.408	0.412	0.404	0.389	0.399
Pr	0.042	0.038	0.042	0.042	0.043	0.041	0.043	0.044	0.045	0.044	0.044	0.045
Nd	0.138	0.144	0.147	0.142	0.145	0.136	0.151	0.153	0.155	0.152	0.146	0.147
Sm	0.029	0.030	0.029	0.028	0.031	0.028	0.025	0.026	0.028	0.027	0.027	0.027
Eu	0.004	0.003	0.002	0.004	0.002	0.004	0.006	0.006	0.007	0.007	0.008	0.008
Gd	0.021	0.018	0.022	0.022	0.021	0.020	0.014	0.017	0.019	0.015	0.017	0.016
Tb	0.000	0.000	0.000	0.000	0.000	0.000	0.000	0.000	0.000	0.000	0.000	0.000
Dy	0.008	0.008	0.007	0.007	0.010	0.008	0.003	0.001	0.004	0.001	0.008	0.000
Er	0.001	0.000	0.001	0.000	0.002	0.000	0.000	0.000	0.000	0.000	0.000	0.000
Yb	0.000	0.000	0.001	0.000	0.000	0.000	0.000	0.000	0.000	0.000	0.000	0.000
Y	0.043	0.044	0.044	0.040	0.048	0.045	0.016	0.022	0.033	0.005	0.040	0.006
Ca	0.044	0.065	0.031	0.071	0.044	0.053	0.036	0.043	0.040	0.053	0.041	0.048
Cat. Sum	1.98	1.99	1.98	2.00	1.99	1.98	1.98	1.99	1.99	1.98	1.98	1.98

* T.P. = Textural position of the grain, mic. = microlithon, Sp = main foliation;

**S.P. = EMP Spot Position

Table 3

Sample	Mnz	Spot	Textural	Analysis	Isotope ratios						Apparent ages (Ma)						% Th-Pb disc.*
number	number	location	Position	number	$^{206}Pb/^{238}U$	1s % (Prop)	$^{207}Pb/^{235}U$	1s % (Prop)	$^{208}Pb/^{232}Th$	1s % (Prop)	$^{206}Pb/^{238}U$	1s abs	$^{207}Pb/^{235}U$	1s abs	$^{208}Pb/^{232}Th$	1s abs	
KL-21	Mnz 240	core	main foliation.	JI04a006	0.08102	0.14%	0.70437	2.36%	0.02514	0.05%	502.2	8.8	541.4	18.2	501.9	9.9	0%
KL-21	Mnz 239	core	main foliation	JI04a007	0.00636	0.01%	0.05281	0.22%	0.00194	0.00%	40.9	0.8	52.3	2.2	39.2	0.7	4%
KL-21	Mnz 237	core	in microlithon	JI04a008	0.00684	0.01%	0.08716	0.39%	0.00177	0.00%	43.9	0.9	84.9	3.7	35.7	0.7	19%
KL-21	Mnz 226	rim	main foliation	JI04a009	0.00849	0.02%	0.06370	0.49%	0.00187	0.00%	54.5	1.3	62.7	4.8	37.8	0.9	31%
KL-21	Mnz 226	rim	main foliation	JI04a010	0.00637	0.01%	0.05415	0.28%	0.00198	0.00%	40.9	0.8	53.5	2.8	40.0	0.9	2%
KL-21	Mnz 228	rim	in microlithon	JI04a011	0.00670	0.01%	0.05764	0.32%	0.00158	0.00%	43.0	0.9	56.9	3.1	31.9	0.6	26%
KL-21	Mnz 229	rim	main foliation	JI04a012	0.00532	0.01%	0.04358	0.16%	0.00175	0.00%	34.2	0.6	43.3	1.6	35.3	0.7	-3%
KL-21	Mnz 229	rim	main foliation	JI04a013	0.00568	0.01%	0.04721	0.22%	0.00178	0.00%	36.5	0.7	46.8	2.1	35.9	0.7	2%
KL-21	Mnz 242	core	in microlithon	JI04a014	0.00495	0.01%	0.03895	0.15%	0.00145	0.00%	31.8	0.6	38.8	1.5	29.3	0.6	8%
KL-21	Mnz 217	rim	in microlithon	JI04a015	0.00574	0.01%	0.04549	0.21%	0.00180	0.00%	36.9	0.7	45.2	2.1	36.3	0.7	1%
KL-21	Mnz 216	rim	main foliation	JI04a016	0.00568	0.01%	0.04702	0.19%	0.00178	0.00%	36.5	0.7	46.7	1.9	35.9	0.7	2%
KL-21	Mnz 216	rim	main foliation	JI04a017	0.00590	0.01%	0.04796	0.17%	0.00187	0.00%	37.9	0.7	47.6	1.7	37.8	0.7	0%
KL-21	Mnz 218	rim	main foliation	JI04a020	0.00490	0.01%	0.04404	0.21%	0.00152	0.00%	31.5	0.6	43.8	2.1	30.7	0.6	3%
KL-21	Mnz 212	rim	main foliation	JI04a021	0.00601	0.01%	0.04699	0.20%	0.00187	0.00%	38.6	0.7	46.6	2.0	37.8	0.7	2%
KL-21	Mnz 209	rim	main foliation	JI04a022	0.00626	0.01%	0.05054	0.19%	0.00184	0.00%	40.2	0.7	50.1	1.9	37.2	0.7	8%
KL-21	Mnz 208	rim	main foliation	JI04a024	0.00538	0.01%	0.04364	0.23%	0.00166	0.00%	34.6	0.7	43.4	2.3	33.5	0.7	3%
KL-21	Mnz 206	core	in microlithon	JI04a026	0.00571	0.01%	0.04803	0.22%	0.00175	0.00%	36.7	0.7	47.6	2.1	35.3	0.7	4%
KL-21	Mnz 204	rim	in microlithon	JI04a027	0.00417	0.01%	0.04341	0.19%	0.00129	0.00%	26.8	0.5	43.1	1.9	26.1	0.6	3%
KL-21	Mnz 203	rim	in microlithon	JI04a028	0.01072	0.02%	0.08327	0.41%	0.00182	0.00%	68.7	1.3	81.2	4.0	36.8	0.7	47%
KL-21	Mnz 201	rim	main foliation	JI04a029	0.00613	0.01%	0.05576	0.24%	0.00188	0.00%	39.4	0.8	55.1	2.4	38.0	0.7	4%
KL-21	Mnz 201	rim	main foliation	JI04a030	0.00613	0.01%	0.04533	0.16%	0.00187	0.00%	39.4	0.7	45.0	1.6	37.8	0.7	4%
KL-19	Mnz 301	rim	in staurolite	JI04b006	0.00533	0.01%	0.04270	0.14%	0.00186	0.00%	34.3	0.6	42.5	1.4	37.6	0.5	-9.6%
KL-19	Mnz 304	rim	main foliation	JI04b009	0.00582	0.01%	0.04524	0.13%	0.00183	0.00%	37.4	0.6	44.9	1.2	37.0	0.5	1.2%
KL-19	Mnz 306	core	in microlithon	JI04b010	0.00588	0.01%	0.05253	0.12%	0.00179	0.00%	37.8	0.7	52.0	1.2	36.1	0.5	4.4%
KL-19	Mnz 307	rim	In magnetite	JI04b011	0.00479	0.01%	0.03086	0.10%	0.00151	0.00%	30.8	0.5	30.9	1.0	30.5	0.4	1.0%
KL-19	Mnz 308	rim	main foliation	JI04b012	0.00637	0.01%	0.04944	0.15%	0.00195	0.00%	40.9	0.7	49.0	1.4	39.4	0.7	3.8%
KL-19	Mnz 308	rim	main foliation	JI04b013	0.00643	0.01%	0.04187	0.11%	0.00202	0.00%	41.3	0.7	41.6	1.1	40.8	0.7	1.3%
KL-19	Mnz 311	rim	main foliation	JI04b015	0.00564	0.01%	0.03922	0.11%	0.00173	0.00%	36.3	0.6	39.1	1.1	34.9	0.5	3.6%
KL-19	Mnz 311	rim	main foliation	JI04b016	0.00571	0.01%	0.04748	0.15%	0.00175	0.00%	36.7	0.6	47.1	1.5	35.3	0.5	3.7%
KL-19	Mnz 313	rim	in microlithon	JI04b017	0.00576	0.01%	0.04163	0.10%	0.00181	0.00%	37.0	0.6	41.4	1.0	36.6	0.5	1.3%
KL-19	Mnz 317	rim	main foliation	JI04b018	0.00623	0.01%	0.04728	0.11%	0.00205	0.00%	40.0	0.7	46.9	1.1	41.4	0.7	-3.4%
KL-19	Mnz 317	rim	main foliation	JI04b019	0.00601	0.01%	0.04784	0.12%	0.00194	0.00%	38.6	0.7	47.4	1.2	39.2	0.7	-1.4%
KL-19	Mnz 319	rim	main foliation	JI04b020	0.00648	0.01%	0.05056	0.14%	0.00205	0.00%	41.6	0.7	50.1	1.4	41.4	0.7	0.6%
KL-19	Mnz 319	rim	main foliation	JI04b021	0.00642	0.01%	0.05122	0.15%	0.00204	0.00%	41.3	0.7	50.7	1.5	41.2	0.7	0.2%
KL-19	Mnz 322	rim	main foliation	JI04b023	0.00467	0.01%	0.03758	0.11%	0.00153	0.00%	30.0	0.5	37.5	1.1	30.9	0.5	-2.9%
KL-19	Mnz 330	rim	main foliation	JI04b025	0.00464	0.01%	0.03634	0.12%	0.00145	0.00%	29.8	0.6	36.2	1.2	29.3	0.4	1.9%
KL-19	Mnz 334	rim	in garnet	JI04b027	0.00681	0.01%	0.05160	0.18%	0.00216	0.00%	43.8	0.8	51.1	1.8	43.6	0.7	0.3%
KL-19	Mnz 334	core	in garnet	JI04b028	0.00708	0.01%	0.05196	0.17%	0.00221	0.00%	45.5	0.8	51.4	1.7	44.6	0.7	1.9%
KL-19	Mnz 334	rim	in garnet	JI04b029	0.00754	0.02%	0.05575	0.29%	0.00241	0.00%	48.4	1.0	55.1	2.9	48.7	0.9	-0.5%
KL-19	Mnz 332	core	main foliation	JI04b030	0.00537	0.01%	0.04173	0.14%	0.00166	0.00%	34.5	0.6	41.5	1.4	33.5	0.5	2.9%

* Prop = propagated error

** % Th-Pb disc. = % of Th-Pb discordance

Table 4

Spot Name	% Pbc	U (ppm)	Th (ppm)	$^{232}Th/^{238}U$	$^{207}Pb/^{235}U$	1 sigma %	$^{206}Pb/^{238}U$	1 sigma %	errcorr	^{207}Pb-corrected $^{206}Pb/^{238}U$	1 sigma	^{207}Pb-corrected $^{206}Pb/^{238}U$ age	1 sigma	Zoning
KL19-312.1	2.43	3582	19644	5.7	0.011162	42.8	0.0027128	2.13	0.05	0.002770	0.000045	17.8	0.3	unzoned
KL19-312.2	0.84	3340	21237	6.6	0.031580	9.6	0.0048082	1.62	0.17	0.004802	0.000074	30.9	0.5	unzoned
KL21-216.1	1.96	1920	33047	17.8	0.022079	28.7	0.0050137	1.88	0.07	0.005107	0.000083	32.8	0.5	rim
KL19-308.1	1.80	4179	26781	6.6	0.037137	8.7	0.0053770	1.55	0.18	0.005354	0.000081	34.4	0.5	rim
KL21-216.2	1.08	2847	49706	18.0	0.026413	14.7	0.0054342	1.62	0.11	0.005513	0.000086	35.4	0.6	rim
KL19-307	1.03	2701	17622	6.7	0.034664	10.5	0.0055063	1.60	0.15	0.005514	0.000084	35.4	0.5	unzoned
KL19-308.3	0.90	3694	21494	6.0	0.036107	12.5	0.0056928	1.62	0.13	0.005698	0.000084	36.6	0.5	rim
KL21-212	1.39	2536	44690	18.2	0.035865	14.2	0.0059520	1.66	0.12	0.005975	0.000091	38.4	0.6	unzoned
KL21-4	0.80	2052	27504	13.8	0.028114	23.6	0.0059299	1.87	0.08	0.006023	0.000098	38.7	0.6	unzoned
KL21-201.1	2.09	3703	62310	17.4	0.015617	59.3	0.0059001	1.93	0.03	0.006106	0.000096	39.2	0.6	unzoned
KL19-317.2	0.64	4701	34309	7.5	0.025332	20.8	0.0061216	1.64	0.08	0.006252	0.000094	40.2	0.6	rim
KL19-317.1	1.09	4044	31074	7.9	0.033934	11.4	0.0062471	1.64	0.14	0.006306	0.000100	40.5	0.6	rim
KL21-216.3	1.06	3555	61072	17.8	0.037972	13.7	0.0063039	1.71	0.12	0.006329	0.000101	40.7	0.6	core
KL19-301	1.18	3501	76746	22.6	0.038289	13.3	0.0064700	1.66	0.12	0.006502	0.000100	41.8	0.6	rim
KL19-330	0.77	3883	25415	6.8	0.036640	11.2	0.0065488	1.57	0.14	0.006601	0.000099	42.4	0.6	unzoned
KL19-308.2	0.21	3706	24947	7.0	0.043585	7.3	0.0070936	1.53	0.21	0.007115	0.000107	45.7	0.7	core

Pbc : common lead